

Dark Matter and Collider Phenomenology in Radiative Type-III Seesaw Model with Two Inert Doublets

Tapender*, Labh Singh† and Surender Verma‡

Department of Physics and Astronomical Science, Central University of Himachal Pradesh,
Dharamshala-176215, INDIA

Abstract

We investigate a minimal Type-III scotogenic model featuring two inert scalar doublets and a hyperchargeless triplet fermion. The scalar sector, in addition to the Standard Model Higgs, includes a rich spectrum of dark scalars comprising two CP-even, two CP-odd, and two charged states. This framework gives rise to two viable dark matter candidates: the lightest CP-even dark scalar and the neutral component of the triplet fermion. We perform a comprehensive analysis of both dark matter scenarios, carefully examining their viability under the umbrella of theoretical consistency conditions and experimental constraints. Beyond the conventional collider signatures anticipated in the Type-III scotogenic model with a single inert doublet, our extended framework predicts distinctive and novel signatures.

1 Introduction

Two of the most profound mysteries in the Standard Model (SM) of particle physics are the origin of neutrino masses and the nature of dark matter. Neutrino oscillation experiments have firmly established that neutrinos have small but nonzero masses [1–4], challenging the SM framework where neutrinos are massless. Similarly, the observed relic density of dark matter (DM), measured with remarkable precision by cosmic microwave background (CMB) experiments [5], indicates the existence of a stable, non-luminous component of the Universe that cannot be explained by SM particles alone. These compelling clues strongly suggest the need for new physics beyond the SM.

The Type-III scotogenic model, first proposed by Ma [6], elegantly addresses the origin of neutrino masses and the nature of dark matter by introducing a discrete Z_2 symmetry and new particles: an

*tapenderphy@gmail.com

†sainilabh5@gmail.com

‡s_7verma@hpcu.ac.in

inert scalar doublet (ϕ) and three hyperchargeless ($Y = 0$) triplet fermions (Σ) [7]. All these fields are odd under the Z_2 symmetry, which prevents neutrino masses at tree level and ensures the stability of the lightest Z_2 -odd particle, making it a natural dark matter candidate. Neutrino masses arise from quantum loop corrections involving the inert scalar and triplet fermions, with their smallness explained by the heavy right-handed fermion scale and loop suppression, making the scotogenic model a compelling SM extension. Also, due to the Z_2 symmetry, the triplet fermion decouple from the neutrino sector and its neutral component could be a viable fermionic DM candidate which satisfies the relic density bound for $M_{\Sigma^0} \simeq 2.5$ TeV [7]. In this framework, achieving the correct relic density requires a relatively large Yukawa coupling in the term $y\tilde{\phi}^\dagger\bar{\Sigma}L$, which can be realized by imposing a near-degeneracy between the CP-even and CP-odd components of the inert scalar, resulting in a highly suppressed quartic coupling $\lambda_5 \sim 10^{-9} - 10^{-10}$ [8, 9]. Moreover, the scalar DM scenario in this model resembles the inert doublet model (IDM) [10–25], which is tightly constrained by DM direct detection experiments [26], making the IDM highly fine-tuned. A possible resolution to this issue involves extending the scalar sector of the Type-III scotogenic model. In this context, several extensions of the minimal scotogenic model [27–31] have been explored, where the scalar sector is augmented with additional singlet [32–38], inert doublet [39–43] and triplet scalar [44–49]. Also, due to its $SU(2)$ triplet nature, the triplet fermion in Type-III scotogenic model exhibits enhanced gauge interactions, leading to a higher production cross-section and distinct visible decay modes. This makes it a compelling candidate for experimental searches at colliders. Recent studies demonstrate that using fat-jet techniques, triplet fermions with high masses can be explored at LHC [50].

We explore an extension of the Type-III scotogenic model by introducing an additional inert scalar doublet. Neutrino masses are generated at the one-loop level, which requires at least one triplet fermion, resulting in a framework with two inert doublets and a triplet fermion. In this setup, we examine both scalar and fermion dark matter scenarios. During the radiation-dominated era, a triplet fermion DM with a mass below 2.5 TeV tends to be under-abundant due to large annihilation and co-annihilation cross-sections into electroweak gauge bosons and fermions, resulting in a delayed freeze-out. However, the presence of a second inert doublet can significantly alter the dark matter phenomenology, potentially lowering the viable dark matter mass scale. Furthermore, we investigate the phenomenological implications of this model at both e^+e^- and pp colliders. The presence of an additional doublet and a triplet fermion could lead to distinctive signatures at high-energy experiments, including modified production cross-sections, decay channels, and final-state distributions. ATLAS [51] and CMS [52] have established a lower bound on the mass of the triplet fermion at 790 GeV. At higher mass ranges, the production cross-section of the triplet fermion decreases significantly, making it challenging to probe effectively at the LHC. However, triplet fermions with masses as large as 1.5 TeV can still be explored, as shown in Ref. [50]. These collider signatures provide a promising avenue for testing the model and constraining its parameter space through future precision measurements.

The structure of this work is as follows: In Section 2, we present the extension of the Type-III scotogenic model. The theoretical and experimental constraints on the model are outlined in Section 3. Section 4 provides a detailed analysis of both scalar and fermion dark matter scenarios. The collider signatures associated with these dark matter candidates are examined in Section 5. Finally, concluding remarks are given in Section 6.

2 Radiative Type-III Seesaw Model

In our model, we want to study the dark matter (DM) and the origin of neutrino masses by considering a radiative Type-III seesaw model. In general, the minimum number of right-handed fermions required to get correct neutrino masses is two. However, we can make another setup in which we can just use only one right-handed fermion as shown in [40–42]. For this, we need to add one more inert scalar to the particle content. This not only allows us to generate neutrino mass, but with the addition of another inert scalar, the DM analysis is also modified as new particles open up various new channels. We have extended the Standard Model (SM) with two inert doublets ϕ_k ($k = 1, 2$) and one fermionic triplet Σ . Abelian discrete Z_2 symmetry is used to separate the dark sector from the SM sector. Under this symmetry, all SM particles are even and all new particles are odd. The transformations under Z_2 symmetry can be written as:

$$\Sigma \rightarrow -\Sigma, \quad \phi_k \rightarrow -\phi_k, \quad \Phi \rightarrow \Phi, \quad \Psi_{\text{SM}} \rightarrow \Psi_{\text{SM}},$$

where Ψ_{SM} denotes all the SM fermions and Φ denotes SM Higgs doublet.

The relevant part of Yukawa Lagrangian can be written as

$$-\mathcal{L}_Y = y_{k,\alpha} \tilde{\phi}_k^\dagger \bar{\Sigma} L_\alpha + \frac{M_\Sigma}{2} \text{Tr}(\bar{\Sigma} \Sigma^c) + \text{H.c.}, \quad (1)$$

where $\alpha = e, \mu, \tau$ represent charged leptons, $k = 1, 2$ and M_Σ denote the mass of fermion triplet. The symbol L_α denote left-handed lepton doublet and $y_{k,\alpha}$ denote Yukawa couplings of neutrinos and triplet fermion with inert scalar ϕ_k . Also, $\tilde{\phi}_k = i\sigma_2 \phi_k^*$ where σ_2 is Pauli spin matrix and $\Sigma^c = C\bar{\Sigma}^T$, C is the charge conjugation matrix and fermion triplet, in $SU(2)$ representation, can be written as [7]

$$\Sigma = \begin{pmatrix} \frac{\Sigma^0}{\sqrt{2}} & \Sigma^+ \\ \Sigma^- & -\frac{\Sigma^0}{\sqrt{2}} \end{pmatrix}, \quad (2)$$

where Σ^0 and Σ^\pm have same mass M_Σ , at the tree level.

The scalar potential of our model under the exact Z_2 symmetry can be written as [39]

$$\begin{aligned} V(\Phi, \phi_k) = & -\mu_\Phi^2 \Phi^\dagger \Phi + \frac{1}{6} \lambda_\Phi (\Phi^\dagger \Phi)^2 + \mu_k^2 \phi_k^\dagger \phi_k + \frac{1}{6} \lambda_k (\phi_k^\dagger \phi_k)^2 \\ & + \kappa_k (\Phi^\dagger \Phi) (\phi_k^\dagger \phi_k) + \zeta_k (\phi_k^\dagger \Phi) (\Phi^\dagger \phi_k) + \omega_1 (\phi_1^\dagger \phi_1) (\phi_2^\dagger \phi_2) + \omega_2 (\phi_2^\dagger \phi_1) (\phi_1^\dagger \phi_2) \\ & + \left[\mu_3^2 \phi_1^\dagger \phi_2 + \frac{1}{2} \eta_k (\Phi^\dagger \phi_k)^2 + \eta_3 (\Phi^\dagger \phi_1) (\Phi^\dagger \phi_2) + \eta_4 (\phi_1^\dagger \Phi) (\Phi^\dagger \phi_2) + \text{H.c.} \right], \end{aligned} \quad (3)$$

where $k = 1, 2$ and all scalar couplings are real parameters.

The scalar doublets can be parameterized as,

$$\Phi = \begin{pmatrix} \xi^+ \\ \frac{1}{\sqrt{2}}(v + h + i\xi^0) \end{pmatrix}, \quad \phi_k = \begin{pmatrix} \chi_k^+ \\ \frac{1}{\sqrt{2}}(\chi_k^0 + iS_k^0) \end{pmatrix}; \quad k = 1, 2 \quad (4)$$

where $v = 246$ GeV is the vacuum expectation value (vev), h is CP-even Higgs field, ξ^+ and ξ^0 are charged and CP-odd parts, respectively, of Higgs doublet. In inert sector we have χ_k^0 and S_k^0 which are CP-even and CP-odd parts, respectively, and χ_k^+ represent charged components of ϕ_k . After electroweak symmetry breaking (EWSB), we have mass eigenstates which consists of two CP-even states $H_{1,2}^0$, two CP-odd states $A_{1,2}^0$ and two pairs of charged scalars $H_{1,2}^\pm$. The mass eigenstates are related to gauge eigenstates as,

$$\begin{pmatrix} H_1^0 \\ H_2^0 \end{pmatrix} = \begin{pmatrix} c_H & s_H \\ -s_H & c_H \end{pmatrix} \begin{pmatrix} \chi_1^0 \\ \chi_2^0 \end{pmatrix}, \quad \begin{pmatrix} A_1^0 \\ A_2^0 \end{pmatrix} = \begin{pmatrix} c_A & s_A \\ -s_A & c_A \end{pmatrix} \begin{pmatrix} S_1^0 \\ S_2^0 \end{pmatrix}, \quad \begin{pmatrix} H_1^\pm \\ H_2^\pm \end{pmatrix} = \begin{pmatrix} c_C & s_C \\ -s_C & c_C \end{pmatrix} \begin{pmatrix} \chi_1^\pm \\ \chi_2^\pm \end{pmatrix}, \quad (5)$$

where $c_Y = \cos \theta_Y$, $s_Y = \sin \theta_Y$ with θ_H , θ_A and θ_C are mixing angles for CP-even, CP-odd and charged scalars, respectively. In this work, we assume the hierarchy among the masses of inert scalars as $m_{H_1^0} < m_{A_1^0} < m_{H_1^\pm} < m_{H_2^0} < m_{A_2^0} < m_{H_2^\pm}$ to study dark matter phenomenology.

The scalar couplings can be written in terms of masses of inert scalars

$$\begin{aligned} \mu_1^2 &= m_{H_1^\pm}^2 c_C^2 + m_{H_2^\pm}^2 s_C^2 - \frac{1}{2} \kappa_1 v^2, \quad \mu_2^2 = m_{H_1^\pm}^2 s_C^2 + m_{H_2^\pm}^2 c_C^2 - \frac{1}{2} \kappa_2 v^2, \\ \mu_3^2 &= c_C s_C (m_{H_2^\pm}^2 - m_{H_1^\pm}^2), \\ \zeta_1 &= \frac{1}{v^2} (m_{H_1^0}^2 c_H^2 + m_{H_2^0}^2 s_H^2 + m_{A_1^0}^2 c_A^2 + m_{A_2^0}^2 s_A^2 - 2(m_{H_1^\pm}^2 c_C^2 + m_{H_2^\pm}^2 s_C^2)), \\ \zeta_2 &= \frac{1}{v^2} (m_{H_2^0}^2 c_H^2 + m_{H_1^0}^2 s_H^2 + m_{A_2^0}^2 c_A^2 + m_{A_1^0}^2 s_A^2 - 2(m_{H_2^\pm}^2 c_C^2 + m_{H_1^\pm}^2 s_C^2)), \\ \eta_1 &= \frac{1}{v^2} ((m_{H_1^0}^2 c_H^2 + m_{H_2^0}^2 s_H^2) - (m_{A_1^0}^2 c_A^2 + m_{A_2^0}^2 s_A^2)), \\ \eta_2 &= \frac{1}{v^2} ((m_{H_1^0}^2 s_H^2 + m_{H_2^0}^2 c_H^2) - (m_{A_1^0}^2 s_A^2 + m_{A_2^0}^2 c_A^2)), \\ \eta_3 &= \frac{1}{v^2} (s_H c_H (m_{H_2^0}^2 - m_{H_1^0}^2) - s_A c_A (m_{A_2^0}^2 - m_{A_1^0}^2)), \\ \eta_4 &= \frac{1}{v^2} (s_H c_H (m_{H_2^0}^2 - m_{H_1^0}^2) + s_A c_A (m_{A_2^0}^2 - m_{A_1^0}^2) - 2c_C s_C (m_{H_2^\pm}^2 - m_{H_1^\pm}^2)). \end{aligned} \quad (6)$$

So, free parameters of our model are $\kappa_{1,2}$, $y_{k,\alpha}$, $m_{H_{1,2}^0}$, $m_{A_{1,2}^0}$, $m_{H_{1,2}^\pm}$, M_Σ and $s_{H,A,C}$.

The Yukawa Lagrangian part consisting of inert scalar fields can be written, in terms of their mass eigenstates, as

$$\begin{aligned} -\mathcal{L}_Y &= \sum_{\alpha,k} \left[\frac{1}{2} (g_{k\alpha} H_k^0 + i f_{k\alpha} A_k^0) \bar{\Sigma}^0 \nu_{\alpha L} - h_{k\alpha} H_k^\pm \bar{\Sigma}^\pm \nu_{\alpha L} \right. \\ &\quad \left. + \frac{1}{\sqrt{2}} (g_{k\alpha} H_k^0 + i f_{k\alpha} A_k^0) \bar{\Sigma}^- l_{\alpha L} + \frac{1}{\sqrt{2}} h_{k\alpha} H_k^\pm \bar{\Sigma}^0 l_{\alpha L} \right] + \text{H.c.}, \end{aligned} \quad (7)$$

with $\alpha = e, \mu, \tau$ and $k = 1, 2$

$$\begin{aligned} g_{1\alpha} &= c_H y_{1,\alpha} + s_H y_{2,\alpha}, \quad g_{2\alpha} = -s_H y_{1,\alpha} + c_H y_{2,\alpha}, \\ f_{1\alpha} &= c_A y_{1,\alpha} + s_A y_{2,\alpha}, \quad f_{2\alpha} = -s_A y_{1,\alpha} + c_A y_{2,\alpha}, \\ h_{1\alpha} &= c_C y_{1,\alpha} + s_C y_{2,\alpha}, \quad h_{2\alpha} = -s_C y_{1,\alpha} + c_C y_{2,\alpha}. \end{aligned} \quad (8)$$

The first two terms inside parenthesis in Eqn. (7) induce neutrino mass at the one-loop level through the radiative seesaw mechanism. The third term, can contribute to the neutrino transition magnetic moment, while the last three terms play a role in lepton flavor violating decays.

After EWSB, the light neutrino mass generated at one-loop level can be expressed as

$$m_{\alpha\beta}^{(\nu)} = \sum_{k=1}^2 M_{\Sigma} \left\{ g_{k\alpha} g_{k\beta} \mathcal{F}\left(\frac{m_{H_k^0}}{M_{\Sigma}}\right) - f_{k\alpha} f_{k\beta} \mathcal{F}\left(\frac{m_{A_k^0}}{M_{\Sigma}}\right) \right\}, \quad (9)$$

with loop factor $\mathcal{F}(x) = \frac{x^2 \log(x)}{8\pi^2(x^2-1)}$.

The neutrino mass matrix can be written as,

$$(m^{\nu})_{3\times 3} = (y^T)_{3\times 2} (\Lambda)_{2\times 2} (y)_{2\times 3}, \quad (10)$$

where y is Yukawa coupling matrix and Λ is a non-diagonal matrix which consists of loop factors

$$\Lambda = \begin{pmatrix} \Lambda_{11} & \Lambda_{12} \\ \Lambda_{12} & \Lambda_{22} \end{pmatrix}, \quad (11)$$

$$\begin{aligned} \Lambda_{11} &= M_{\Sigma} \left[c_H^2 \mathcal{F}\left(\frac{m_{H_1^0}}{M_{\Sigma}}\right) + s_H^2 \mathcal{F}\left(\frac{m_{H_2^0}}{M_{\Sigma}}\right) - c_A^2 \mathcal{F}\left(\frac{m_{A_1^0}}{M_{\Sigma}}\right) - s_A^2 \mathcal{F}\left(\frac{m_{A_2^0}}{M_{\Sigma}}\right) \right], \\ \Lambda_{12} &= M_{\Sigma} \left[s_H^2 \mathcal{F}\left(\frac{m_{H_1^0}}{M_{\Sigma}}\right) + c_H^2 \mathcal{F}\left(\frac{m_{H_2^0}}{M_{\Sigma}}\right) - s_A^2 \mathcal{F}\left(\frac{m_{A_1^0}}{M_{\Sigma}}\right) - c_A^2 \mathcal{F}\left(\frac{m_{A_2^0}}{M_{\Sigma}}\right) \right], \\ \Lambda_{22} &= M_{\Sigma} \left[c_H s_H \left(\mathcal{F}\left(\frac{m_{H_1^0}}{M_{\Sigma}}\right) - \mathcal{F}\left(\frac{m_{H_2^0}}{M_{\Sigma}}\right) \right) - c_A s_A \left(\mathcal{F}\left(\frac{m_{A_1^0}}{M_{\Sigma}}\right) - \mathcal{F}\left(\frac{m_{A_2^0}}{M_{\Sigma}}\right) \right) \right]. \end{aligned} \quad (12)$$

Using Casas-Ibarra parameterization [53], we have Yukawa coupling matrix

$$y = U_{\Lambda} D_{\sqrt{\Lambda}}^{-1} R D_{\sqrt{m}} U^{\dagger}, \quad (13)$$

where U_{Λ} and $D_{\sqrt{\Lambda}}$ are diagonalizing and diagonal matrix for Λ , respectively. The diagonal neutrino mass matrix and Pontecorvo-Maki-Nakawaga-Sakata (PMNS) neutrino mixing matrix are denoted by $D_{\sqrt{m}}$ and U , respectively, and R is orthogonal matrix with complex angle θ . In this model, the lightest neutrino remains massless. We will consider normal hierarchy of neutrino masses, so R can be written as,

$$R = \begin{pmatrix} 0 & \cos \theta & \sin \theta \\ 0 & -\sin \theta & \cos \theta \end{pmatrix}. \quad (14)$$

3 Constraints: Theoretical and Experimental

This model need to satisfy some theoretical and experimental constraints which we have discussed as follows:

Theoretical constraints: The couplings of the scalar potential need to satisfy the following theoretical constraints:

- **Vacuum Stability:** To ensure that in all directions of field space scalar potential is bounded from below we need scalar couplings to satisfy some constraints [39, 54–57]: $\lambda_\Phi > 0$, $\lambda_1 > 0$, $\lambda_2 > 0$, $\lambda_\Phi \lambda_1 \lambda_2 - \lambda_\Phi [\min(0, \omega_1 + \omega_2)]^2 - \lambda_2 \min(0, \kappa_1 + \zeta_1 + \eta_1) + 2 \min(0, \omega_1 + \omega_2) \min(0, \kappa_1 + \zeta_1 + \eta_1) \min(0, \kappa_2 + \zeta_2 + \eta_3) - \lambda_1 [\min(0, \kappa_2 + \zeta_2 + \eta_2)]^2 > 0$, $\frac{8\lambda_\Phi \lambda_1 \lambda_2}{27} - \frac{2}{3} \lambda_2 [\min(0, \kappa_1 + \zeta_1)]^2 - \frac{2}{3} \lambda_\Phi [\min(0, \omega_1 + \omega_2)]^2 + 2 \min(0, \kappa_1 + \zeta_1) \min(0, \omega_1 + \omega_2) \min(0, \kappa_2 + \zeta_2) - \frac{2}{3} \lambda_1 [\min(0, \kappa_2 + \zeta_2)]^2 > 0$. In addition to this, we also require, $\mu_1^2 > 0$, $\mu_2^2 > 0$, $\mu_1^2 + \mu_2^2 - \sqrt{(\mu_2^2 - \mu_1^2)^2 + 4(\mu_3^2)^2} > 0$.
- **Perturbativity:** For theory to remain in the perturbative regime we need scalar couplings to satisfy the following bounds: λ_Φ , $\lambda_{1,2}$, $|\kappa_{1,2}|$, $|\kappa_{1,2} + \zeta_{1,2}|$, $|\zeta_{1,2} + \kappa_{1,2} \pm \eta_{1,2}|$, $|\omega_1|$, $|\omega_1 + \omega_2|$, $|\eta_{1,2}|$, $\frac{1}{2}|\zeta_{1,2} \pm \eta_{1,2}|$, $\frac{1}{2}|\omega_2| \leq 4\pi$.
- **Perturbative unitarity:** All processes involving scalars or gauge bosons, perturbative unitarity need to be preserved. It is shown in Ref. [58] that when eigenvalues (Λ_i) of scattering amplitude matrix are smaller than 8π i.e., $|\Lambda_i| < 8\pi$ perturbative unitarity conditions are achieved. In the models like we are investigating here, the full scattering amplitude matrix can be divided into six sub-matrices due to presence of some exact symmetries like CP, electric charge and global Z_2 symmetry. These sub-matrices and their basis are given in Ref. [39].

Experimental constraints:

- **Gauge bosons decay widths:** The decay widths of W/Z bosons are measured with high precision at LEP and we do not want it to change due to decay of W/Z bosons to Z_2 odd scalars. This can be achieved if we assume that $\min(m_{H_1^\pm} + m_{A_1^0}, m_{H_1^\pm} + m_{H_1^0}) > m_W$, $\min(m_{H_1^0} + m_{A_1^0}, 2m_{H_1^\pm}) > m_Z$, $M_{\Sigma^0} + M_{\Sigma^\pm} > m_W$, $2M_{\Sigma^\pm} > m_Z$. Here, m_W and m_Z denote the masses of the W and Z bosons, respectively, while M_{Σ^0} and M_{Σ^\pm} represent the masses of the neutral and charged components of the triplet fermion.
- **LEP direct searches of charginos and neutralinos:** The lower bounds on the masses of light neutral inert scalars (H_1^0 , A_1^0) and charged inert scalar H_1^\pm can be put by considering the null results of neutralinos and charginos searches at LEP [59]. We have considered $\max(m_{A_1^0}, m_{H_1^0}) > 110$ GeV and $m_{H_1^\pm} > 78$ GeV [60, 61].
- **Lepton flavor violating (LFV) processes:** We have also considered the LFV bound for the $\mu \rightarrow e\gamma$ process, which gives the most stringent upper bound for the branching ratio $Br(\mu \rightarrow e\gamma) < 4.2 \times 10^{-13}$ [62]. The lepton flavor processes are induced at the one-loop level to which the triplet fermion along with the inert scalars gives a contribution [7].
- **Electroweak precision observables:** We require that the oblique parameters S , T and U remain within the following ranges: $S = -0.04 \pm 0.10$, $T = 0.01 \pm 0.12$ and $U = -0.01 \pm 0.09$, in order to maintain consistency with electroweak precision data [63].

- **Neutrino oscillation data:** Neutrino oscillation data within the 3σ range [64] is used for the calculation of Yukawa couplings using the Casas-Ibarra parameterization (see Eqn. 13). Thus, our model is consistent with neutrino oscillation data.

4 Dark Matter Phenomenology

For the dark matter, we have two candidates in this model, *i.e.*, either the neutral inert scalar H_1^0 or the neutral component of the triplet fermion Σ^0 . Now, we will investigate the dark matter phenomenology of the model by considering both scenarios one by one. For this, we will make use of the SARAH toolchain. First, we have implemented the model in SARAH-4.15.2 [65–68] and generated the modules for SPheno-4.0.5 [69, 70] and micrOMEGAs-5.3.41 [71–75]. SPheno-4.0.5 numerically calculates the mass spectrum, LFV observables, vertices, etc., while micrOMEGAs-5.3.41 computes the cold dark matter (CDM) relic density along with the spin-independent DM direct detection cross-section. In the following analysis, the free scalar couplings are kept within the range $0 \leq |\kappa_{1,2}| \leq 4\pi$, the mixing angles are varied such that $|s_{H,A,C}| \leq 1$ and Yukawa couplings $y_{i\alpha}$ with strength $\sqrt{4\pi} > |y_{i\alpha}| \geq 10^{-4}$ are considered.

4.1 Scalar Dark Matter

We have studied dark matter phenomenology in the scalar sector by considering the neutral CP-even particle H_1^0 as dark matter (DM). As mentioned earlier, the hierarchy among the inert scalar particles is set to $m_{H_1^0} < m_{A_1^0} < m_{H_1^\pm} < m_{H_2^0} < m_{A_2^0} < m_{H_2^\pm}$. We have studied three cases considering different co-annihilation scenarios of DM as shown in Table 1 [76]. In all cases, mass of triplet fermion is the largest. The mass of triplet fermion is varied considering lower bound of 790 GeV from ATLAS and CMS experiments. For higher mass region of DM due to perturbativity and unitarity conditions we need to have small mass splitting among inert scalar particles, so co-annihilation are unavoidable. However, to avoid co-annihilation in low mass region in different cases the mass range for the particle next to DM particle or its co-annihilating partner (CoP) is kept such that their mass splitting $(M_{Heavy} - M_{DM/CoP})/M_{DM/CoP} \geq 0.20$, hence there will be no unwanted co-annihilation upto 250 GeV mass of DM particle (see Table 1).

The relic density (Ωh^2) of DM obtained for various cases considered in Table 1 is shown in Fig. 1 as a function of DM mass. The light green points indicate under abundant DM relic density, red-star points lie within the observed 3σ range [5] and the gray-triangle points represent over abundant relic density. The black horizontal lines correspond to the experimental 3σ range of DM relic density [5].

In case I only annihilation of H_1^0 is present upto 250 GeV as masses of other inert scalars and triplet fermion are higher (see Table 1). For this case DM mass versus the relic density (Ωh^2) plot is shown in

Fig. 1(a).

Mass (GeV)	Case I	Case II	Case III
$m_{H_1^0}$	1 – 3000	1 – 3000	1 – 3000
$m_{A_1^0}$	$m_{H_1^0} + (50 - 150)$	$m_{H_1^0} + (0.001 - 5)$	$m_{H_1^0} + (0.001 - 5)$
$m_{H_1^\pm}$	$m_{A_1^0} + (2 - 50)$	$m_{A_1^0} + (0.001 - 5)$	$m_{A_1^0} + (0.001 - 5)$
$m_{H_2^0}$	$m_{H_1^\pm} + (2 - 50)$	$m_{H_1^\pm} + (0.001 - 5)$	$m_{H_1^\pm} + (0.001 - 5)$
$m_{A_2^0}$	$m_{H_2^0} + (2 - 50)$	$m_{H_2^0} + (0.001 - 5)$	$m_{H_2^0} + (0.001 - 5)$
$m_{H_2^\pm}$	$m_{A_2^0} + (2 - 50)$	$m_{A_2^0} + (50 - 150)$	$m_{A_2^0} + (0.001 - 5)$
M_Σ	$m_{H_2^\pm} + (700 - 1500)$	$m_{H_2^\pm} + (700 - 1500)$	$m_{H_2^\pm} + (700 - 1500)$

Table 1: Mass ranges for different dark sector particles in various cases for inert scalar dark matter.

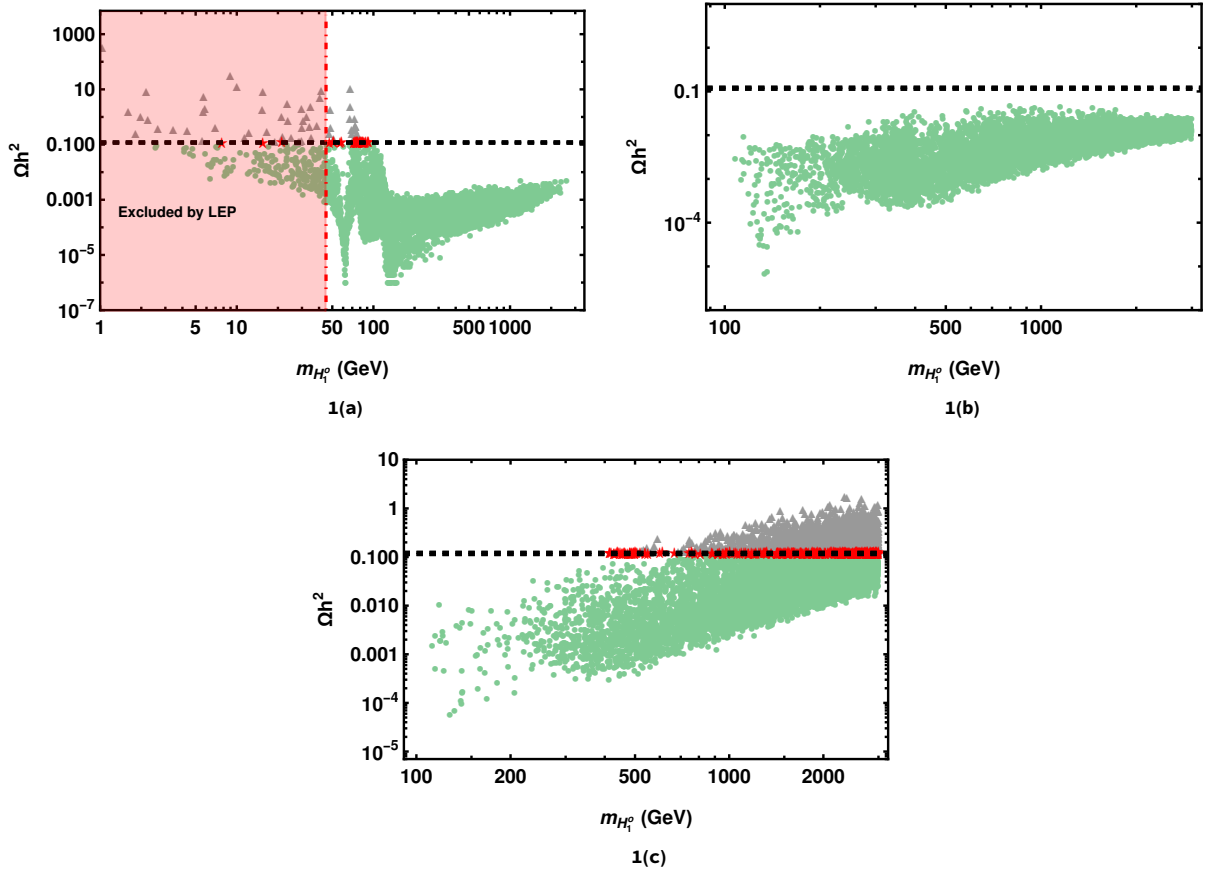


Figure 1: Figures 1(a) to 1(c) show the results obtained for CDM relic density for cases I to III, as listed in Table 1, respectively. Light green points indicate an under abundant dark matter region, red stars correspond to values within the observed 3σ range, and gray triangles represent an over abundant relic density. The black horizontal lines correspond to the experimental 3σ range, while the red shaded region in Fig. 1(a) is excluded by LEP data.

As evident from this figure, in lower DM mass region upto the 100 GeV, the relic density can be under abundant, over abundant or lie within the experimental 3σ region. However, region of DM mass upto 45 GeV is excluded by the LEP data, shown by the red shaded region, this sets a lower bound on the DM

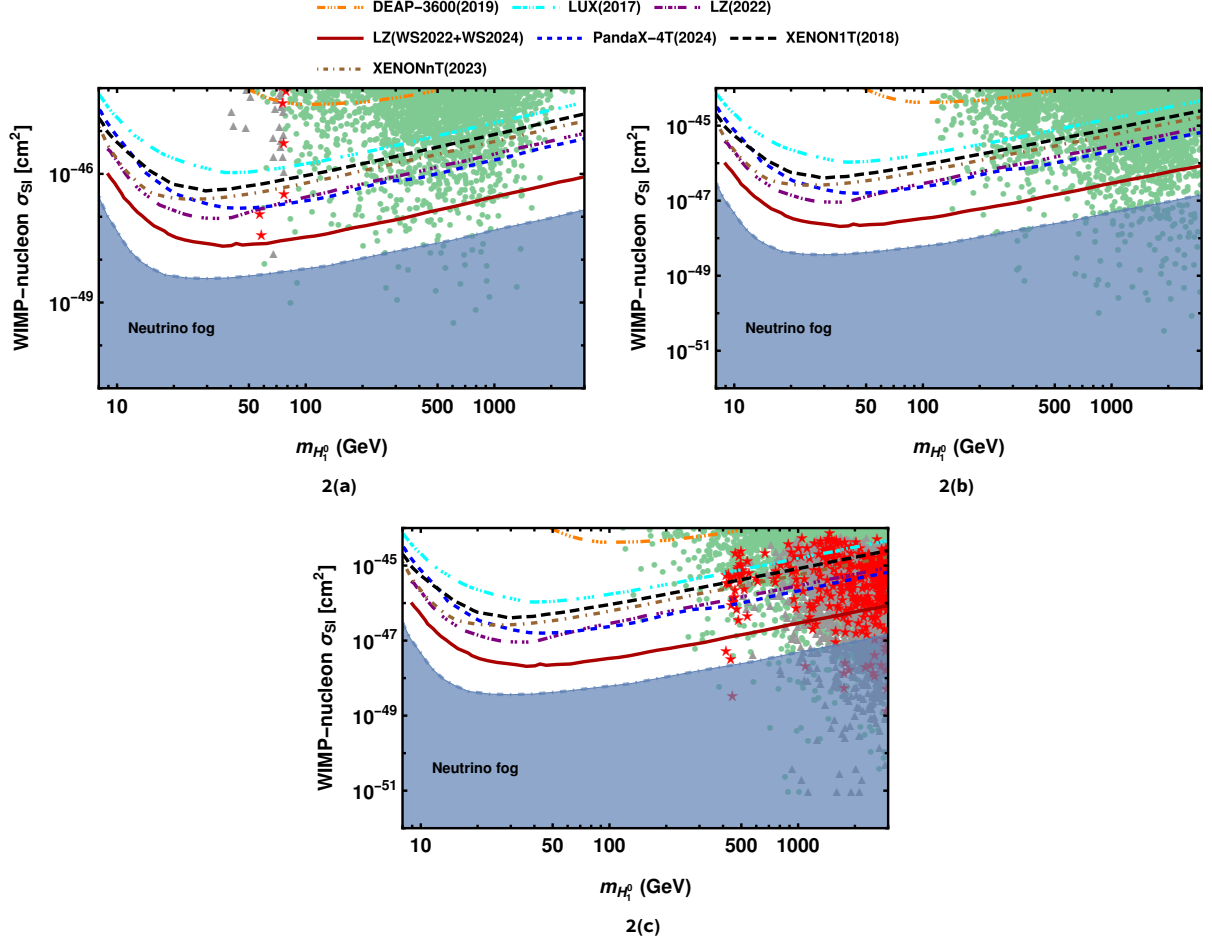


Figure 2: The spin-independent nucleon–dark matter cross-section for cases I (2(a)), II (2(b)) and III (2(c)). The color coding is same as in Fig. 1.

mass. We will only consider DM mass region which lies above it. Around Higgs-resonance region, where DM mass is half of the mass of Higgs particle m_h (*i.e.*, $m_{DM} \approx m_h/2 \approx 62$ GeV), we have a sharp dip. This is due to the Higgs mediated s -channel annihilation processes, in which $DM+DM \rightarrow h \rightarrow SM+SM$. The annihilation diagrams of type Figs. 12(a) and 12(b) dominantly contributes in this region (with S being DM particle H_1^0). However, DM annihilation through t -channel processes mediated by charged components of triplet fermion Σ^\pm to charged leptons also gives contribution in this region shown in Fig. 12(c). In the region around the mass of W/Z boson (m_{W^\pm}/m_Z) *i.e.*, $m_{H_1^0} = m_{W^\pm} = 80$ GeV and $m_{H_1^0} = m_Z = 92$ GeV, annihilation processes shown in Figs. 12(d) to 12(f) dominates with W^\pm/Z in the final states. Another dip occurs as the mass of DM reaches around mass of Higgs approximately 125 GeV. In this region DM annihilation to Higgs particles dominates, the processes are shown in Figs. 12(g) and 12(h). After this region processes where DM annihilates to Higgs particle h and W^\pm/Z bosons dominates, which continues in higher mass region where co-annihilation processes such as shown in Fig. 13 can take place. So, in high mass region of DM all processes shown from Figs. 12 to 13, giving Higgs particle h and W^\pm/Z bosons keep occurring which keeps the relic density under abundant. These features are similar to the inert doublet model or Scotogenic model with one inert doublet. Here, relic density remains under abundant for higher DM mass. The under abundant region obtained in this case is not disallowed but requires another partner to satisfy the observed relic density value. Now to achieve the correct relic density at higher masses we will consider the co-annihilation cases as the presence of co-annihilation processes can increase or decrease the DM relic density by affecting the effective (co-)annihilation cross-section of DM.

So, in case II all inert scalars except for H_2^\pm can co-annihilate starting from the lower DM mass. Now, because of experimental constraints on masses as discussed in Section 3, lower mass of DM is not allowed, as evident from Fig. 1(b). From this figure we can see that, in all range of DM mass relic density is under abundant. However, the relic density of DM is increased in the higher mass region in comparison to the case I. This implies that effective cross-section of DM (co-)annihilation is reduced. The dominating channels and processes remain the same as in case I with addition of co-annihilation processes. So, in higher mass region, main contribution comes from the DM to Higgs, W^\pm and Z (with their combinations like hh , $W^\pm W^\mp$, ZZ , hW^\pm and ZW^\pm). The relevant annihilation and co-annihilation processes are shown in Figs. 12-16.

In case III, all inert scalar particles are close in mass and thus can co-annihilate starting from lower DM mass region. Relic density and DM mass plot is shown in Fig. 1(c). The (co-)annihilation processes dominating are similar to case II. As, evident from this figure that we have regions where relic density is under abundant, lying in 3σ range and over abundant. In this case, we have region of DM mass starting around 414 GeV where DM relic density constraint can be satisfied (shown by red-star points). This is one of the features of a model with two inert doublets [77]. In comparison to the inert doublet model or Scotogenic model with one inert doublet, where DM relic density in the high mass region is satisfied above 500 GeV, here it can be as low as 414 GeV. This new region with low DM mass

can have implications for searches of new particles in collider experiments. We will see this possibility later in this paper. The impact of decreasing the value of mass splitting among inert scalars can be seen in Figs. 1(b) and 1(c). More co-annihilating partners with appropriate value of mass splitting allow the relic density to reach near the experimentally observed region of CDM relic density. All inert scalar particles can be almost degenerate with each other, this leads to the reduction of effective (co-)annihilation cross-section of DM. This reduction increases CDM relic abundance and we can even cross the experimentally observed region of CDM relic density.

The spin-independent (SI) WIMP-nucleon cross-section (σ_{SI}) as a function of the DM mass, $m_{H_1^0}$, for all cases listed in Table 1 are shown in Figs. 2(a) to 2(c), respectively. The upper limits from various dark matter direct detection experiments such as: combined LUX-ZEPLIN (LZ) WIMP Search 2024 and 2022 (WS2024+WS2022) analysis [26], LZ (2022) [78], LUX [79], PandaX-4T [80] (all power-constrained to -1σ), XENONnT [81] (reinterpreted with a -1σ power constraint), XENON1T [82] and DEAP-3600 [83] are, also, shown. The blue shaded area in the figure corresponds to “neutrino fog” region [84].

From these plots, it is evident that under the most stringent upper limit, which arises from the LZ WS2024+WS2022 analysis, the majority of parameter space is excluded. In case I for low DM mass region, as the Higgs dark matter coupling required in this region to satisfy the relic density is large which makes it difficult to reconcile it with SI WIMP-nucleon cross-section bound. However, for case III, in higher mass region a significant number of points which satisfies experimental 3σ bound on relic density of DM, remain within the allowed region.

4.2 Fermionic Dark Matter

We have studied the DM phenomenology of fermionic DM which in this model is the neutral component Σ^0 of fermion triplet Σ . At tree level all components of triplet fermion are mass degenerate. However, a small mass splitting arises between the neutral and charged components when one loop correction to mass is considered [6]. This makes the Σ^0 slightly lighter among other components and thus makes it a DM candidate. We have studied two cases of DM co-annihilation. For this study, we have followed the following mass hierarchy among the dark sector particles: $M_\Sigma < m_{H_1^0} < m_{A_1^0} < m_{H_1^\pm} < m_{H_2^0} < m_{A_2^0} < m_{H_2^\pm}$. Here, also, the mass of triplet fermion is varied keeping in mind the lower bound of 790 GeV from ATLAS and CMS experiments.

In case I, we have studied only (co-)annihilations among components of triplet fermion as mass of neutral component Σ^0 and charged components Σ^\pm are close to each other. However, by choosing the appropriate mass difference between lightest inert scalar particle and fermion triplet we have avoided the co-annihilations of triplet fermions with inert scalars. For this purpose we have varied the mass of H_1^0 such that its mass splitting with triplet fermion is ≥ 0.20 i.e., $(m_{H_1^0} - M_\Sigma)/M_\Sigma \geq 0.20$ in whole

Mass (GeV)	Case I	Case II
M_Σ	700 – 3000	700 – 3000
$m_{H_1^0}$	$1.2M_\Sigma$ to $(1.2M_\Sigma + 100)$	$M_\Sigma + (0.001 - 5)$
$m_{A_1^0}$	$m_{H_1^0} + (2 - 5)$	$m_{H_1^0} + (0.001 - 5)$
$m_{H_1^\pm}$	$m_{A_1^0} + (2 - 5)$	$m_{A_1^0} + (0.001 - 5)$
$m_{H_2^0}$	$m_{H_1^\pm} + (2 - 5)$	$m_{H_1^\pm} + (0.001 - 5)$
$m_{A_2^0}$	$m_{H_2^0} + (2 - 5)$	$m_{H_2^0} + (0.001 - 5)$
$m_{H_2^\pm}$	$m_{A_2^0} + (2 - 5)$	$m_{A_2^0} + (0.001 - 5)$

Table 2: Mass ranges for different dark sector particles in two cases for fermionic dark matter.

range of DM mass. The other inert scalar particles automatically satisfy this condition because of mass hierarchy we have chosen. The masses are varied as shown in second column of Table 2. The results for DM relic density as a function of DM mass, after satisfying all the constraints mentioned in Section 3, are shown in Fig. 3(a). In the plots shown in Fig. 3, the color and shape classification of the points has the same meaning as mentioned previously. The various (co-)annihilation processes of DM are shown in Fig. 17.

The DM relic density is satisfied for region starting around 2332 GeV to 2452 GeV of DM mass. This obtained region for DM mass matches with the region mentioned in Ref. [6], where SM is extended by a single triplet fermion without considering neutrino mass. Now we propose a scenario wherein co-annihilation processes with inert scalars can lower the region of DM mass.

In case II, all inert scalar particles are closer in mass to the M_Σ and can have co-annihilation with fermion triplet. The masses are varied as shown in third column of Table 2. The result for this case is shown in Fig. 3(b). The various (co-)annihilation processes of DM relevant for this case are shown in Fig. 17 and Fig. 18. Yukawa couplings will play an important role as fermion triplet and inert scalars interaction depends on them. Large Yukawa couplings lead to the tension with the experimental upper bound on $\text{BR}(\mu \rightarrow e\gamma)$. The region where the relic density of DM lies within the experimental 3σ region now begins from a lower DM mass value, around 1483 GeV to 2112 GeV. This is possible due to additional co-annihilation processes of triplet fermion with inert scalar particles as shown in Fig. 18. This is remarkable, as in this case, the mass of the fermion triplet can be around 1483 GeV, which has significant implications for collider searches of the triplet fermion. This will be discussed in the next section.

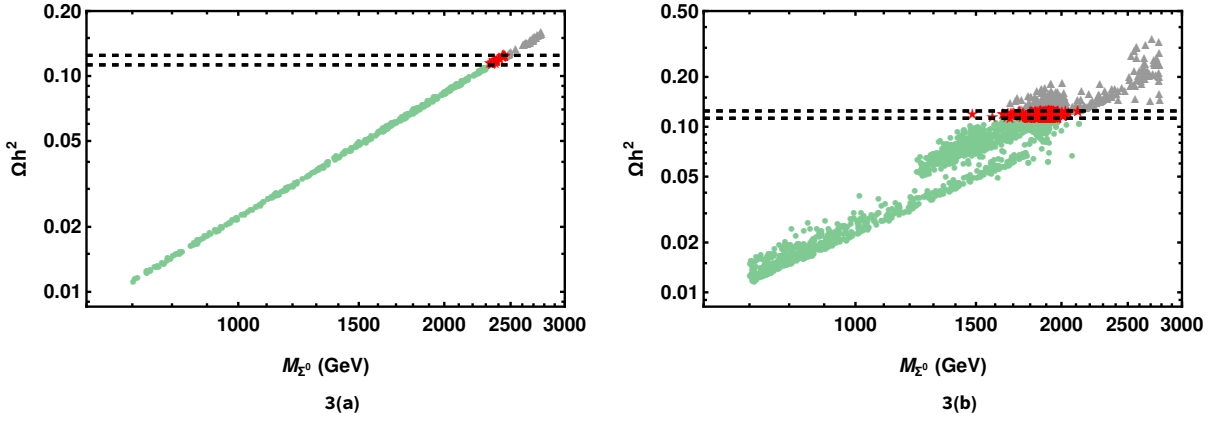


Figure 3: Figures 3(a) and 3(b) show the results obtained for CDM relic density for (co-)annihilation with fermion triplet components only and with all inert scalars, respectively. Light green points indicate an under abundant dark matter region, red stars correspond to values within the observed 3σ range, and gray triangles represent an over abundant relic density. Black horizontal lines mark the experimental 3σ range.

5 Collider Phenomenology

The model contains six inert scalars ($H_{1,2}^0, A_{1,2}^0, H_{1,2}^\pm$) along with fermion triplet Σ ($\Sigma^0, \Sigma^+, \Sigma^-$). Their production at the collider gives us the opportunity to explore the possibility of detection in the collider experiments [8, 13, 25, 50, 85–92]. Here, we focus on production of these particles in future linear e^+e^- collider experiments like CLIC (Compact Linear Collider) which will be designed for center-of-mass energies 380 GeV, 1.5 TeV and 3 TeV [93], with integrated luminosities of 1 ab^{-1} , 2.5 ab^{-1} and 5 ab^{-1} respectively and ILC (International Linear Collider) designed for center-of-mass energy 500 GeV with integrated luminosity of 4 ab^{-1} [94]. We will also study the production of these particles at LHC (Large Hadron Collider) with center-of-mass energies 7 TeV and 14 TeV along with future hadron colliders: HL-LHC (High Luminosity Large Hadron Collider) with center-of-mass energy 27 TeV [95] and FCC-hh (Future Circular Collider for hadron-hadron collision) with center-of-mass energy 100 TeV [96]. To do the collider study we have used SARAH-4.15.2 [65–68] generated UFO model file [97], which then feed to the MadGraph5_aMC@NLO version 3.5.4 [98] to calculate the production cross-section of the various processes.

The production of particles at colliders depends on their mass. In this light, we explore the collider phenomenology of the newly obtained regions of DM mass in both inert scalar and fermion triplet DM scenarios. We have considered the two benchmark points BP1 and BP2 for H_1^0 as dark matter, as shown in second and third columns of Table 3, respectively. BP1 lies in the low DM mass region with DM particle mass $m_{H_1^0} \approx 60 \text{ GeV}$, this point gives under abundant relic density. However, it contributes more than 50% to the total relic density. While BP2 lies in the newly obtained region of DM mass, with $m_{H_1^0} \approx 414 \text{ GeV}$, which gives DM relic density within 3σ experimental range. In the case where fermion triplet Σ^0 is taken as DM particle, we have considered one benchmark point BP3 which also

Parameters	BP1	BP2	BP3
$m_{H_{1,2}^0}$ (GeV)	(60.370, 122.810)	(414.484, 415.982)	(1483.374, 1554.644)
$m_{A_{1,2}^0}$ (GeV)	(111.724, 131.831)	(414.652, 416.354)	(1483.384, 1554.645)
$m_{H_{1,2}^\pm}$ (GeV)	(115.728, 135.695)	(415.248, 416.943)	(1483.536, 1554.981)
M_{Σ^0} (GeV)	1205.384	1311.494	1482.741
M_{Σ^\pm} (GeV)	1205.384	1311.494	1482.789
$s_{H,A,C}$	(-0.991, 0.943, -0.466)	(0.660, 0.572, -0.048)	(-0.379, -0.818, -0.187)
$\kappa_{1,2}$	(0.010, 0.438)	(-0.073, 0.163)	(0.712, -0.518)
$y_{11}/10^{-3}$	$1.762 + 0.576i$	$0.666 - 2.875i$	$8.479 - 7.572i$
$y_{12}/10^{-3}$	$-0.506 - 3.883i$	$-4.213 + 1.710i$	$-9.479 - 109.451i$
$y_{13}/10^{-3}$	$-3.247 - 3.217i$	$-4.178 + 5.150i$	$-65.597 - 72.573i$
$y_{21}/10^{-3}$	$0.711 - 0.346i$	$-0.997 - 0.592i$	$-55.304 + 7.470i$
$y_{22}/10^{-3}$	$-1.307 - 1.040i$	$0.140 + 1.782i$	$-262.601 + 471.215i$
$y_{23}/10^{-3}$	$-1.949 - 0.022i$	$1.430 + 2.179i$	$67.074 + 475.642i$
Ωh^2	0.090	0.121	0.119
$Br(\mu \rightarrow e\gamma)$	3.4×10^{-21}	8.3×10^{-20}	2.3×10^{-13}
σ_{SI} (cm ²)	8.18×10^{-49}	5.19×10^{-48}	–

Table 3: Benchmark points BP1 (second column) and BP2 (third column) correspond to inert scalar ($m_{H_1^0}$) as dark matter in the low and high mass regions, respectively, while BP3 (fourth column) corresponds to fermion triplet (Σ^0) as dark matter. The elements of the Yukawa coupling matrix y are denoted as y_{ij} , where $i = 1, 2$ and $j = 1, 2, 3$.

lies in the newly obtained DM mass region, with triplet mass M_{Σ^0} around 1483 GeV, which satisfies relic density of DM at 3σ range, this point is shown in the fourth column of Table 3. All benchmark points (BP) satisfy the constraints considered in Section 3. In the following, we discuss in detail the collider phenomenology considering these benchmark points.

5.1 Inert Scalars

As we mentioned earlier, inert scalar sector is very rich in particle content. We have studied the prospects of production of these particles in future e^+e^- collider experiments (CLIC and ILC) and at present and future hadron colliders (LHC, HL-LHC and FCC-hh). The inert scalars can be pair-produced in e^+e^- collisions which can consist of charged inert scalars, neutral inert scalars or charged inert scalar in association with a neutral inert scalar. We have different processes for the production of inert scalars which consists of s -channel (t -channel) exchange of Higgs (h), Z bosons and photon (γ) (Σ^0 and Σ^\pm). The Feynman diagrams for different production modes of the inert scalars are shown in Fig. 4 and inert scalar pairs which can be produced in the final state are shown in Table 4. By considering the BP1 and BP2 shown in Table 3, we obtained the production cross-section for the inert scalars as a function of center-of-mass energy (\sqrt{s}). The processes which does not involve Z boson in s -channel have very small production cross-section. So, we have investigated those s -channel processes which are mediated by Z boson, as shown in Table 4. The production cross-section for these particles in final states as a function of \sqrt{s} is shown in Fig. 5(a) and 5(b) for BP1 and BP2, respectively. The

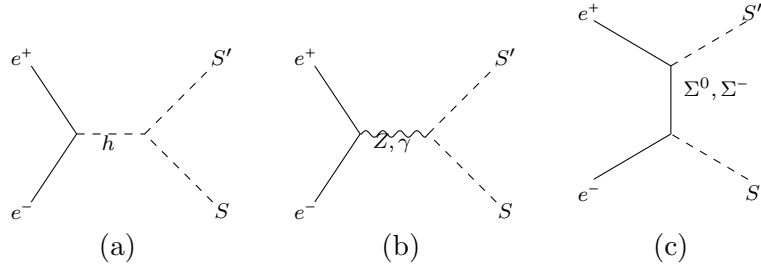


Figure 4: The production modes of the inert scalars at the e^+e^- collider where S and S' belongs to inert scalars (for detail see Table 4).

center-of-mass energy is varied keeping in mind the physics potential of CLIC and ILC experiments. The pair-production cross-section rises sharply after a certain threshold energy. This threshold energy corresponds to the sum of the mass of the produced particles, meaning production is not possible below this energy. As, \sqrt{s} reaches threshold energy phase space for production opens up and cross-section increases sharply. After this peak, cross-section decreases because of the phase space suppression. As evident from the Fig. 5(a), for BP1 production cross-section for the inert scalars pairs $H_1^+ H_1^-$, $H_2^+ H_2^-$ and $H_1^0 A_1^0$ dominates with values around 105 fb (at $\sqrt{s} = 360$ GeV), 76 fb (at $\sqrt{s} = 440$ GeV) and 74 fb (at $\sqrt{s} = 260$ GeV). Since, the masses for BP2 are high, production cross-section reduces and we get its highest value for $H_1^+ H_1^-$ and $H_2^+ H_2^-$ which is 8 fb at $\sqrt{s} = 1.32$ TeV.

We, also, study the production of inert scalars at the LHC and future hadron collider energies HL-LHC and FCC-hh for both benchmark points by varying centre-of-mass energy upto 100 TeV. The various production modes of inert scalar pairs in the final state at pp collider is shown in Fig. 6 and final states are listed in Table 5. These production modes include s -channel processes mediated by Higgs (h), W^\pm boson, Z boson and photon (γ). The final states includes pairs of neutral or charged inert scalars and charged inert scalar in association with neutral ones. We have shown the production cross-section for these inert scalar pairs as a function of \sqrt{s} in left-panel (right-panel) of Fig. 7 for BP1 (BP2). The pair-production cross-section for inert scalars, mediated by W^\pm and Z bosons, is large in comparison to other processes. The cross-sections for various the dominant pairs are shown in Table 6 for BP1 and BP2 at various center-of-mass energies in current and future collider experiments.

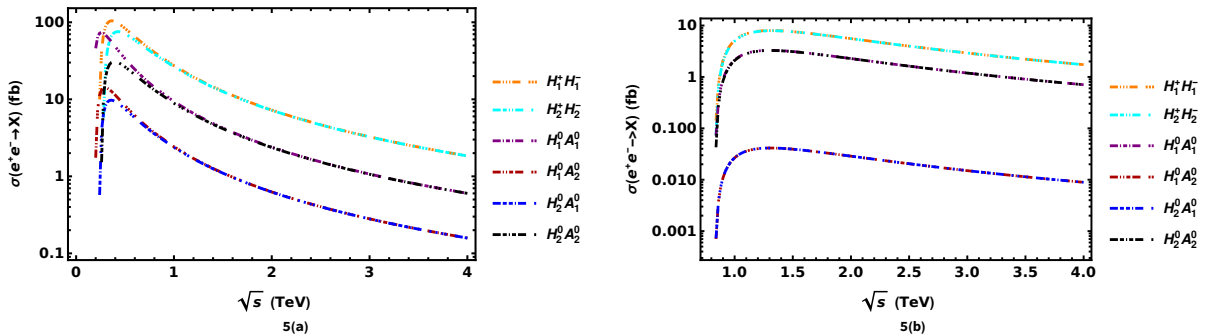


Figure 5: Production cross-section for dominating processes with inert scalars in final state as a function of the center-of-mass energy (\sqrt{s}) in e^+e^- collisions for BP1 (left) and BP2 (right) shown in Table 3.

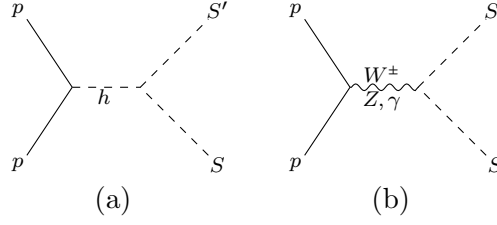


Figure 6: The production modes of the inert scalars at the pp collider where S and S' belongs to inert scalars (for detail see Table 5).

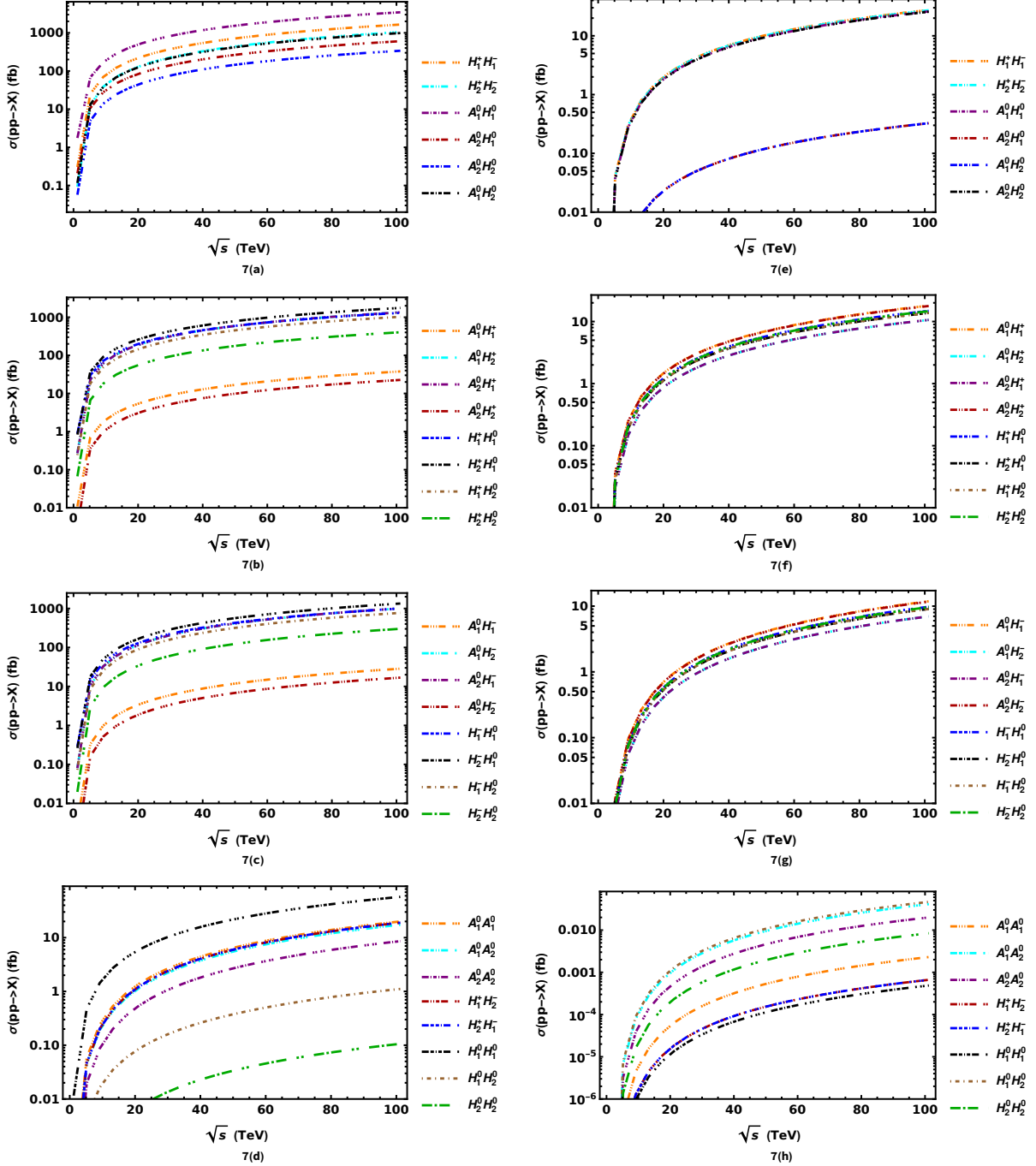


Figure 7: Production cross-section for different inert scalars in final state as a function of the center-of-mass energy (\sqrt{s}) in pp collisions for BP1 (left panel), BP2 (right panel) shown in Table 3.

Mediator	Final state inert scalar pairs (SS')
Higgs (h)	$H_1^+ H_1^-, H_2^+ H_2^-, H_1^+ H_2^-, H_2^+ H_1^-, A_1^0 H_1^0, A_2^0 H_1^0, A_2^0 H_1^0, A_2^0 H_2^0, A_1^0 H_2^0$ $A_2^0 A_2^0, A_1^0 A_1^0, H_1^0 H_1^0, H_2^0 H_2^0, H_1^0 H_2^0, A_1^0 A_2^0$
Z boson	$H_1^+ H_1^-, H_2^+ H_2^-, A_1^0 H_1^0, A_2^0 H_1^0, A_2^0 H_2^0, A_1^0 H_2^0$
Photon (γ)	$H_1^+ H_1^-, H_2^+ H_2^-$
Σ^0	$H_1^- H_1^+, H_2^- H_2^+, H_2^- H_1^+, H_1^- H_2^+$
Σ^-	$H_1^0 A_1^0, H_1^0 A_2^0, A_2^0 H_2^0, A_1^0 H_2^0, A_1^0 H_1^0, A_2^0 H_1^0, A_2^0 H_2^0, A_1^0 H_2^0$ $A_2^0 A_2^0, A_1^0 A_1^0, H_1^0 H_1^0, H_1^0 H_2^0, A_1^0 A_2^0, H_2^0 H_2^0$

Table 4: The inert scalar pairs in final state along with respective mediators in the e^+e^- collision. The Feynman diagrams are shown in Fig. 4.

Mediator	Final state inert scalar pairs (SS')
Higgs (h)	$A_1^0 A_1^0, H_1^+ H_1^-, A_1^0 A_2^0, A_2^0 A_2^0, H_1^+ H_2^-, H_2^+ H_1^-, H_2^+ H_2^-, A_1^0 H_1^0, A_2^0 H_1^0, H_1^0 H_1^0$ $H_1^0 H_2^0, A_1^0 H_2^0, A_2^0 H_2^0, H_2^0 H_2^0$
W^\pm boson	$A_1^0 H_1^\pm, A_1^0 H_2^\pm, A_2^0 H_1^\pm, A_2^0 H_2^\pm, H_1^\pm H_1^0, H_2^\pm H_1^0, H_1^\pm H_2^0, H_2^\pm H_2^0$
Z boson	$H_1^+ H_1^-, H_2^+ H_2^-, A_1^0 H_1^0, A_2^0 H_1^0, A_2^0 H_2^0, A_1^0 H_2^0$
Photon (γ)	$H_1^+ H_1^-, H_2^+ H_2^-$

Table 5: The inert scalar pairs in final state along with their respective mediators in the pp collision. The Feynman diagrams are shown in Fig. 6.

5.2 Fermion Triplet

First, we investigate the production of triplet fermion in e^+e^- collider experiments, such as CLIC and ILC. These particles can be pair-produced in e^+e^- colliders. The production modes for Σ^0 pair include only t -channel with charged inert scalars as mediators and Σ^\pm are pair-produced via s -channel (t -channel) Z boson and photon (γ) (neutral inert scalars) as mediators as shown in Fig. 8. The production cross-section for $\Sigma^\pm \Sigma^\mp$ pair is shown in Fig. 9(a). It is evident that Σ^\pm , cross-section is maximum around $\sqrt{s} = 3.52$ TeV with a value around 13 fb. This lies outside the proposed center-of-mass energy for CLIC and ILC. However, at $\sqrt{s} = 3$ TeV (CLIC center-of-mass energy) we have cross-section around 5 fb. For $\Sigma^0 \Sigma^0$ pair the production cross-section is very small hence, not shown here. This is because of the absence of s -channel production mode. In Fig. 9(b), by considering the lower bound of 790 GeV on triplet fermion mass given by ATLAS and CMS experiments, we have shown the production cross-section for $\Sigma^\pm \Sigma^\mp$ as a function of the triplet fermion pair mass, at CLIC center-of-mass energy, $\sqrt{s} = 3$ TeV.

The production modes for triplet fermions at pp colliders are shown in Fig. 10. Here, we can have pair-production of $\Sigma^\pm \Sigma^\mp$ ($\Sigma^\pm \Sigma^0$) via s -channel exchange of Z boson and photon (γ) (W^\pm boson). The

Particle	LHC 7 TeV		LHC 14 TeV		HL-LHC 27 TeV		FCC-hh 100 TeV	
Pairs	BP1	BP2	BP1	BP2	BP1	BP2	BP1	BP2
$A_1^0 H_1^0$	112	0.12	309	0.85	726	3	3404	25
$H_1^+ H_1^-$	44	0.13	133	0.92	328	4	1625	27
$A_1^0 H_2^0$	9	-	27	-	66	-	334	-
$H_2^+ H_2^-$	24	0.13	76	0.90	197	3	1034	27
$A_2^0 H_1^0$	18	0.12	52	0.83	123	3	595	25
$A_2^0 H_2^0$	24	0.12	75	0.83	189	3	972	25
$H_2^+ H_1^0$	61	-	164	-	380	-	1736	-
$H_2^- H_1^0$	32	-	99	-	253	-	1321	-
$H_1^+ H_1^0$	48	0.09	127	0.60	288	2	1287	15
$H_1^- H_1^0$	26	-	78	-	195	-	988	-
$A_1^0 H_2^+$	40	-	115	-	276	-	1325	-
$A_1^0 H_2^-$	20	-	67	-	179	-	991	-
$A_2^0 H_1^+$	40	-	115	-	277	-	1327	-
$A_2^0 H_1^-$	20	-	67	-	179	-	992	-
$H_1^+ H_2^0$	31	-	89	-	213	-	1013	-
$H_1^- H_2^0$	16	-	52	-	138	-	760	-
$H_2^+ H_2^0$	12	-	34	-	82	-	398	-
$H_2^- H_2^0$	6	-	20	-	53	-	297	-
$A_1^0 H_1^+$	-	0.11	-	0.72	-	3	-	18
$A_2^0 H_2^+$	-	0.11	-	0.70	-	3	-	17

Table 6: Dominating pair-production cross-section (fb) for inert scalars in pp collision at different collider energies for BP1 and BP2. The symbol (-) signifies that the cross-section for the respective pair is small.

production cross-section in pp colliders as a function of \sqrt{s} is shown in Fig. 11(a). The cross-section is found to be very small for low \sqrt{s} and increases with \sqrt{s} . The cross-section of all three pairs is close to each other with $\Sigma^+ \Sigma^0$ dominating with value around 15 fb at $\sqrt{s} = 100$ TeV. In Fig. 11, we have shown the production cross-section of fermion triplet pairs $\Sigma^\pm \Sigma^\mp$ (Fig. 11(b)) and $\Sigma^\pm \Sigma^0$ (Fig. 11(c)) for the HL-LHC and FCC-hh center-of-mass energies, $\sqrt{s} = 27$ TeV and 100 TeV.

We, further, study the signatures that can be seen at colliders from triplet fermion decays. The different decay chains for fermion triplet Σ^\pm and Σ^0 along with their signatures considering inert scalar H_1^0 as DM are shown in Table 7 and 8, respectively. The DM escapes without detection and appears as missing transverse energy (\cancel{E}_T). By, combining these chains we can have signatures in colliders which are tabulated, for $\Sigma^\pm \Sigma^\mp$ and $\Sigma^\pm \Sigma^0$ in Table 9 and 10, respectively. In these tables the same colors of

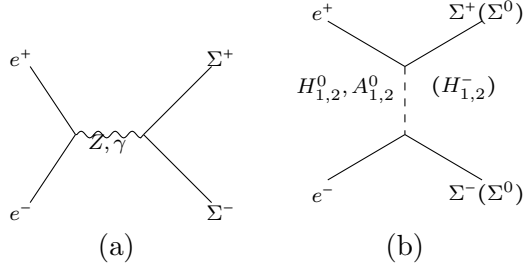


Figure 8: The production modes of the $\Sigma^\pm\Sigma^\mp$ and $\Sigma^0\Sigma^0$ at the e^+e^- collider.

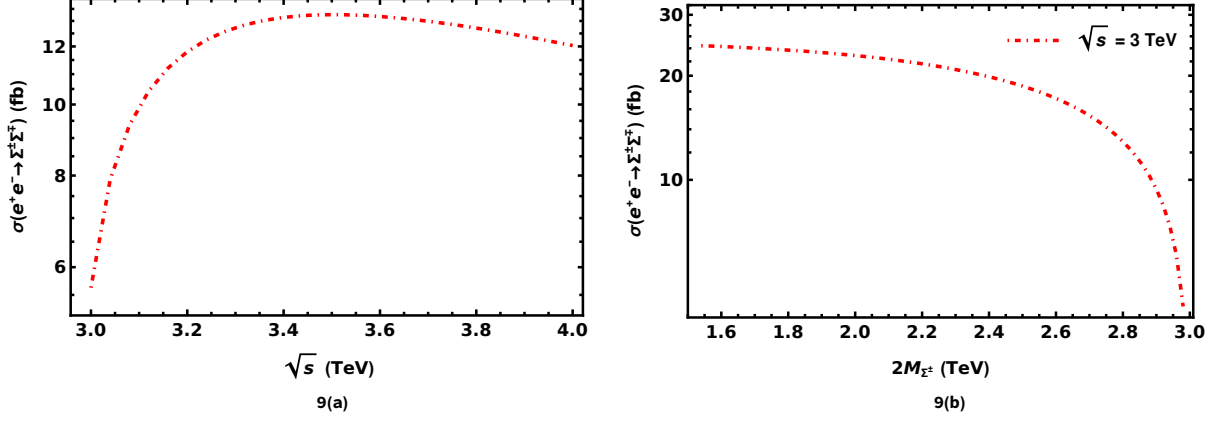


Figure 9: Left panel: pair-production cross-section for $\Sigma^\pm\Sigma^\mp$ as a function of the center-of-mass energy (\sqrt{s}) in e^+e^- collisions for benchmark point BP3, shown in Table 3. Right panel: pair-production cross-section for $\Sigma^\pm\Sigma^\mp$ as a function of the triplet fermion pair mass for CLIC center-of-mass energy (\sqrt{s}), 3 TeV.

different cells shows, which combinations will give us the same signatures at colliders. For the case where Σ^0 is dark matter, Σ^\pm can decay into Σ^0 and a W^\pm boson. The Σ^0 appears as missing transverse energy (\cancel{E}_T). The W^\pm further decays into either a lepton-neutrino pair ($l^\pm\nu_l$) or a quark-antiquark pair (qq'), leading to the signatures $1l + \cancel{E}_T$ and $2j + \cancel{E}_T$, respectively.

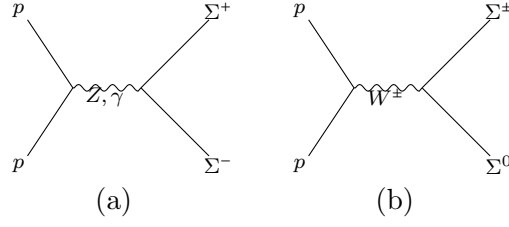


Figure 10: The production modes of the $\Sigma^\pm\Sigma^\mp$ and $\Sigma^0\Sigma^\pm$ at the pp collider.

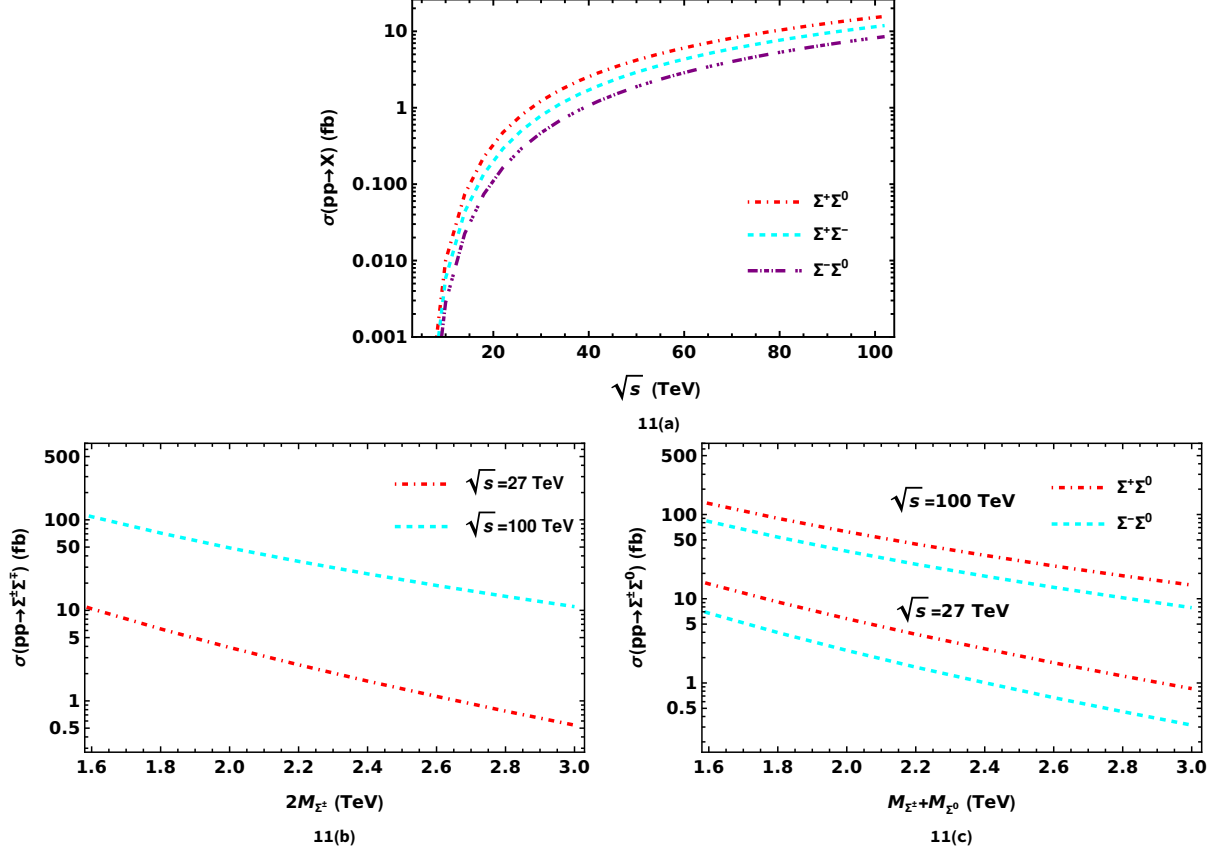


Figure 11: Upper panel: pair-production cross-section for $\Sigma^\pm\Sigma^0$ and $\Sigma^\pm\Sigma^\mp$ as a function of center-of-mass energy (\sqrt{s}) in pp collisions. Lower panel: pair-production cross-section as a function of triplet fermion pair mass at HL-LHC and FCC-hh center-of-mass energy (\sqrt{s}), 27 TeV and 100 TeV.

Mode No.	Decay mode of Σ^\pm	Signature
1	$H_1^0 l^\pm$	$1l + \cancel{E_T}$
2	$(H_2^0/A_1^0/A_2^0)l^\pm \rightarrow H_1^0 h l^\pm \rightarrow H_1^0 q \bar{q}' l^\pm$	$1l + 2j + \cancel{E_T}$
3	$(H_2^0/A_1^0/A_2^0)l^\pm \rightarrow H_1^0 h l^\pm \rightarrow H_1^0 l^+ l'^- l^\pm$	$3l + \cancel{E_T}$
4	$(A_1^0/A_2^0)l^\pm \rightarrow H_1^0 Z l^\pm \rightarrow H_1^0 \nu_l \nu_l l^\pm$	$1l + \cancel{E_T}$
5	$(A_1^0/A_2^0)l^\pm \rightarrow H_1^0 Z l^\pm \rightarrow H_1^0 q \bar{q}' l^\pm$	$1l + 2j + \cancel{E_T}$
6	$(A_1^0/A_2^0)l^\pm \rightarrow H_1^0 Z l^\pm \rightarrow H_1^0 l^+ l^- l^\pm$	$3l + \cancel{E_T}$
7	$(H_1^\pm/H_2^\pm)\nu_l \rightarrow H_1^0 W^\pm \nu_l \rightarrow H_1^0 l^\pm \nu_l \nu_l$	$1l + \cancel{E_T}$
8	$(H_1^\pm/H_2^\pm)\nu_l \rightarrow H_1^0 W^\pm \nu_l \rightarrow H_1^0 q \bar{q}' \nu_l$	$2j + \cancel{E_T}$

Table 7: Decay modes of Σ^\pm along with corresponding signature.

Mode No.	Decay mode of Σ^0	Signature
1'	$H_1^0 \nu_l$	$\cancel{E_T}$
2'	$(H_2^0/A_1^0/A_2^0)\nu_l \rightarrow H_1^0 h \nu_l \rightarrow H_1^0 q \bar{q}' \nu_l$	$2j + \cancel{E_T}$
3'	$(H_2^0/A_1^0/A_2^0)\nu_l \rightarrow H_1^0 h \nu_l \rightarrow H_1^0 l^+ l'^- \nu_l$	$2l + \cancel{E_T}$
4'	$(A_1^0/A_2^0)\nu_l \rightarrow H_1^0 Z \nu_l \rightarrow H_1^0 \nu_l \nu_l \nu_l$	$\cancel{E_T}$
5'	$(A_1^0/A_2^0)\nu_l \rightarrow H_1^0 Z \nu_l \rightarrow H_1^0 q \bar{q} \nu_l$	$2j + \cancel{E_T}$
6'	$(A_1^0/A_2^0)\nu_l \rightarrow H_1^0 Z \nu_l \rightarrow H_1^0 l^+ l^- \nu_l$	$2l + \cancel{E_T}$
7'	$(H_1^\pm/H_2^\pm)l^\mp \rightarrow H_1^0 W^\pm l^\mp \rightarrow H_1^0 l^\pm \nu_l l^\mp$	$2l + \cancel{E_T}$
8'	$(H_1^\pm/H_2^\pm)l^\mp \rightarrow H_1^0 W^\pm l^\mp \rightarrow H_1^0 q \bar{q}' l^\mp$	$1l + 2j + \cancel{E_T}$

Table 8: Decay modes of Σ^0 along with corresponding signature.

$\frac{\Sigma^\mp \rightarrow}{\Sigma^\pm l}$	1	2	3	4	5	6	7	8
1	$2l + \cancel{E_T}$	$2l + 2j + \cancel{E_T}$	$4l + \cancel{E_T}$	$2l + \cancel{E_T}$	$2l + 2j + \cancel{E_T}$	$4l + \cancel{E_T}$	$2l + \cancel{E_T}$	$1l + 2j + \cancel{E_T}$
2	$2l + 2j + \cancel{E_T}$	$2l + 4j + \cancel{E_T}$	$4l + 2j + \cancel{E_T}$	$2l + 2j + \cancel{E_T}$	$2l + 4j + \cancel{E_T}$	$4l + 2j + \cancel{E_T}$	$2l + 2j + \cancel{E_T}$	$1l + 4j + \cancel{E_T}$
3	$4l + \cancel{E_T}$	$4l + 2j + \cancel{E_T}$	$6l + \cancel{E_T}$	$4l + \cancel{E_T}$	$4l + 2j + \cancel{E_T}$	$6l + \cancel{E_T}$	$4l + \cancel{E_T}$	$3l + 2j + \cancel{E_T}$
4	$2l + \cancel{E_T}$	$2l + 2j + \cancel{E_T}$	$4l + \cancel{E_T}$	$2l + \cancel{E_T}$	$3l + 2j + \cancel{E_T}$	$4l + \cancel{E_T}$	$2l + \cancel{E_T}$	$1l + 2j + \cancel{E_T}$
5	$2l + 2j + \cancel{E_T}$	$2l + 4j + \cancel{E_T}$	$4l + 2j + \cancel{E_T}$	$2l + 2j + \cancel{E_T}$	$2l + 4j + \cancel{E_T}$	$4l + 2j + \cancel{E_T}$	$2l + 2j + \cancel{E_T}$	$1l + 4j + \cancel{E_T}$
6	$4l + \cancel{E_T}$	$4l + 2j + \cancel{E_T}$	$6l + \cancel{E_T}$	$4l + \cancel{E_T}$	$4l + 2j + \cancel{E_T}$	$6l + \cancel{E_T}$	$4l + \cancel{E_T}$	$3l + 2j + \cancel{E_T}$
7	$2l + \cancel{E_T}$	$2l + 2j + \cancel{E_T}$	$4l + \cancel{E_T}$	$2l + \cancel{E_T}$	$2l + 2j + \cancel{E_T}$	$4l + \cancel{E_T}$	$2l + \cancel{E_T}$	$1l + 2j + \cancel{E_T}$
8	$1l + 2j + \cancel{E_T}$	$1l + 4j + \cancel{E_T}$	$3l + 2j + \cancel{E_T}$	$1l + 2j + \cancel{E_T}$	$1l + 4j + \cancel{E_T}$	$3l + 2j + \cancel{E_T}$	$1l + 2j + \cancel{E_T}$	$4j + \cancel{E_T}$

Table 9: Possible signatures of $\Sigma^\pm \Sigma^\mp$ pair by combining Σ^\pm (1st column) and Σ^\mp (1st row) signatures for the decays shown in Table 7.

$\frac{\Sigma^0 \rightarrow}{\Sigma^\pm l}$	1'	2'	3'	4'	5'	6'	7'	8'
1	$1l + \cancel{E_l}$	$1l + 2j + \cancel{E_l}$	$3l + \cancel{E_l}$	$1l + \cancel{E_l}$	$1l + 2j + \cancel{E_l}$	$3l + \cancel{E_l}$	$3l + \cancel{E_l}$	$2l + 2j + \cancel{E_l}$
2	$1l + 2j + \cancel{E_l}$	$1l + 4j + \cancel{E_T}$	$3l + 2j + \cancel{E_T}$	$1l + 2j + \cancel{E_T}$	$1l + 4j + \cancel{E_T}$	$3l + 2j + \cancel{E_T}$	$3l + 2j + \cancel{E_T}$	$2l + 4j + \cancel{E_T}$
3	$3l + \cancel{E_l}$	$3l + 2j + \cancel{E_T}$	$5l + \cancel{E_T}$	$3l + \cancel{E_T}$	$3l + 2j + \cancel{E_T}$	$5l + \cancel{E_T}$	$5l + \cancel{E_T}$	$4l + 2j + \cancel{E_T}$
4	$1l + \cancel{E_l}$	$1l + 2j + \cancel{E_T}$	$3l + \cancel{E_T}$	$1l + \cancel{E_T}$	$1l + 2j + \cancel{E_T}$	$3l + \cancel{E_T}$	$3l + \cancel{E_T}$	$2l + 2j + \cancel{E_T}$
5	$1l + 2j + \cancel{E_l}$	$1l + 4j + \cancel{E_T}$	$3l + 2j + \cancel{E_T}$	$1l + 2j + \cancel{E_T}$	$1l + 4j + \cancel{E_T}$	$3l + 2j + \cancel{E_T}$	$3l + 2j + \cancel{E_T}$	$2l + 4j + \cancel{E_T}$
6	$3l + \cancel{E_l}$	$3l + 2j + \cancel{E_T}$	$5l + \cancel{E_T}$	$3l + \cancel{E_T}$	$3l + 2j + \cancel{E_T}$	$5l + \cancel{E_T}$	$5l + \cancel{E_T}$	$4l + 2j + \cancel{E_T}$
7	$3l + \cancel{E_l}$	$3l + 2j + \cancel{E_T}$	$5l + \cancel{E_T}$	$3l + \cancel{E_T}$	$3l + 2j + \cancel{E_T}$	$5l + \cancel{E_T}$	$3l + \cancel{E_T}$	$2l + 2j + \cancel{E_T}$
8	$2l + 2j + \cancel{E_l}$	$2l + 4j + \cancel{E_T}$	$4l + 2j + \cancel{E_T}$	$2l + 2j + \cancel{E_T}$	$2l + 4j + \cancel{E_T}$	$4l + 2j + \cancel{E_T}$	$2l + 2j + \cancel{E_T}$	$1l + 4j + \cancel{E_T}$

Table 10: Possible signatures for $\Sigma^\pm \Sigma^0$ pair by combining Σ^\pm (1st column) and Σ^0 (1st row) signatures for the decays shown in Table 7 and Table 8, respectively.

6 Conclusions

In this work, we explore an extended radiative Type-III scotogenic model featuring two inert scalar doublets and a fermion triplet, where neutrino masses arise at the one-loop level with both inert doublets circulating in the loop. The scalar sector, in addition to the SM Higgs, consists of a rich spectrum of dark scalars: two CP-even, two CP-odd, and two charged states. This framework accommodates two viable DM candidates: the CP-even inert scalar H_1^0 and the neutral component of the triplet fermion Σ^0 . A comprehensive analysis of dark matter phenomenology reveals new viable mass regions where the observed DM relic density is satisfied for both scenarios, shaped by intricate co-annihilation dynamics. In the inert scalar DM scenario, a significant parameter space emerges below 500 GeV—a region often dubbed the “desert region” in the conventional inert doublet model. In the fermionic DM scenario, a new viable region is identified for DM mass below 2.5 TeV. These regions materialize under specific mass hierarchies, where all inert scalars remain nearly degenerate with the DM candidate (Case III for inert scalar DM and Case II for triplet fermion DM in Table 1).

We have also explored the collider implications of the model at both pp and e^+e^- colliders, focusing on the missing energy signatures of the triplet fermion. At higher mass scale, the production cross-section of triplet fermion drops significantly, making detection challenging at the LHC with $\sqrt{s} = 13$ TeV. However, at a future 100 TeV proton-proton collider like FCC-hh, the production cross-section remains substantially high, offering a promising avenue for discovery. This enhancement, as shown in the upper panel of Fig. 11, underscores the FCC-hh’s potential to probe the triplet fermion. Further, we also explored the possible signatures of the triplet fermion at e^+e^- collider, such as ILC and CLIC. Tables 9 and 10 comprise the possible signatures of triplet fermion at both pp and e^+e^- colliders.

Acknowledgments

Tapender acknowledges the financial support provided by Central University of Himachal Pradesh in the form of freeship. LS acknowledges the financial support provided by the Council of Scientific and

Appendix A Feynman diagrams for various processes

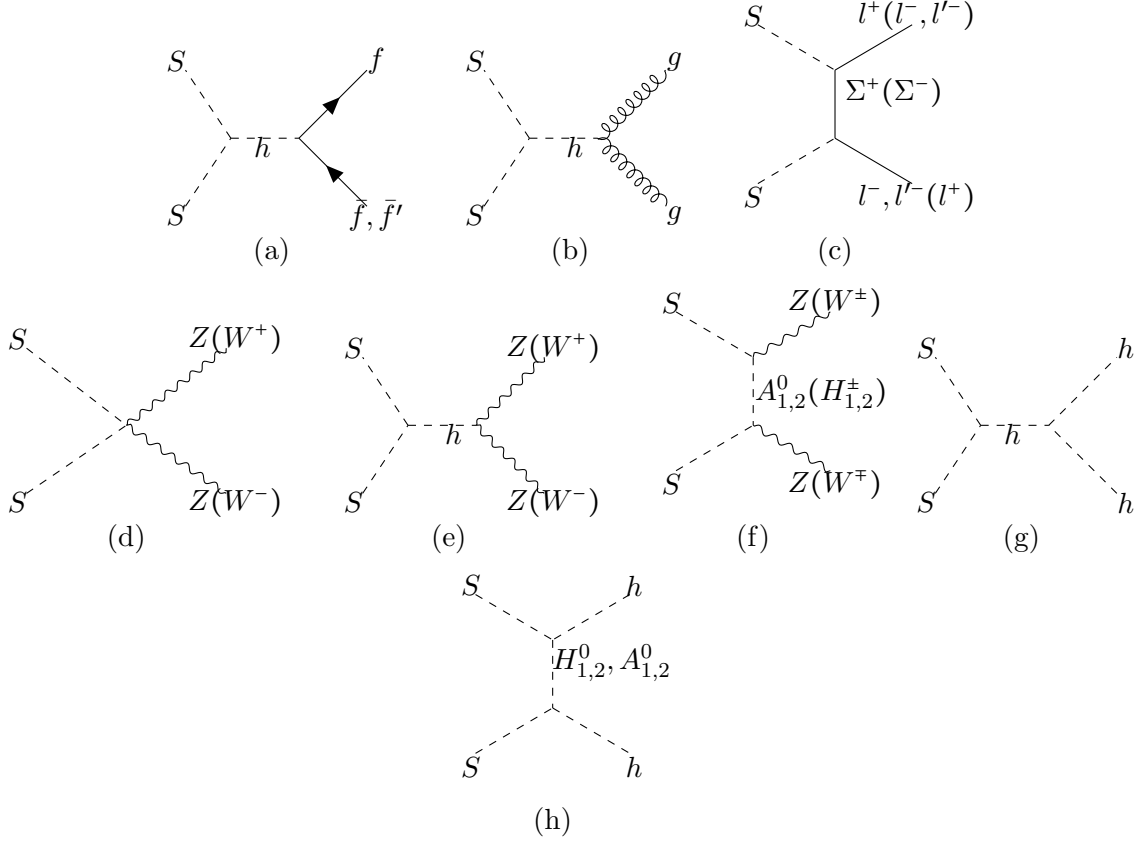


Figure 12: Dominating annihilation channels where S can be $H_{1,2}^0, A_{1,2}^0$, where f (l) represent quark (lepton).

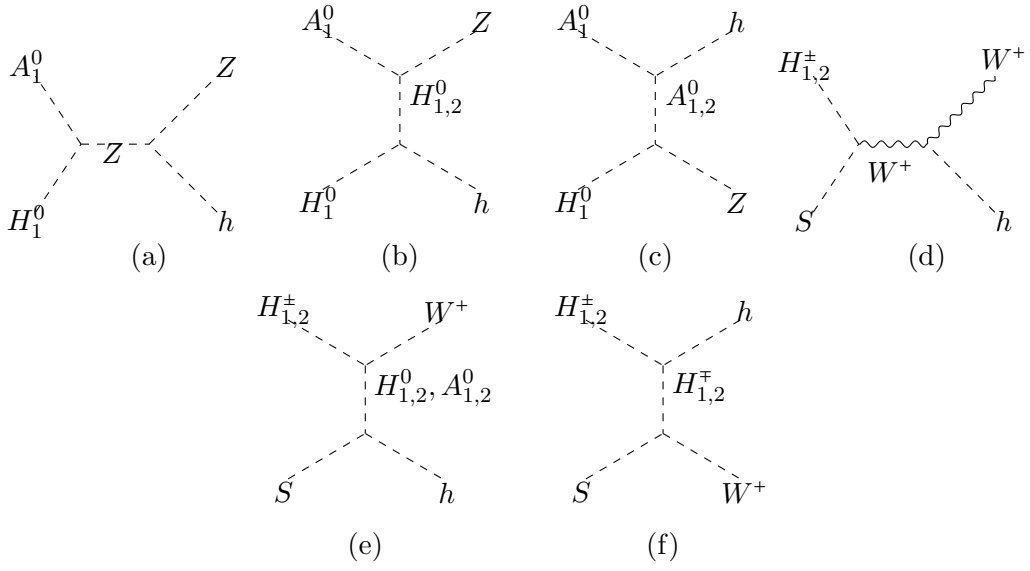


Figure 13: Dominating co-annihilation channels where S can be $H_{1,2}^0, A_{1,2}^0$.

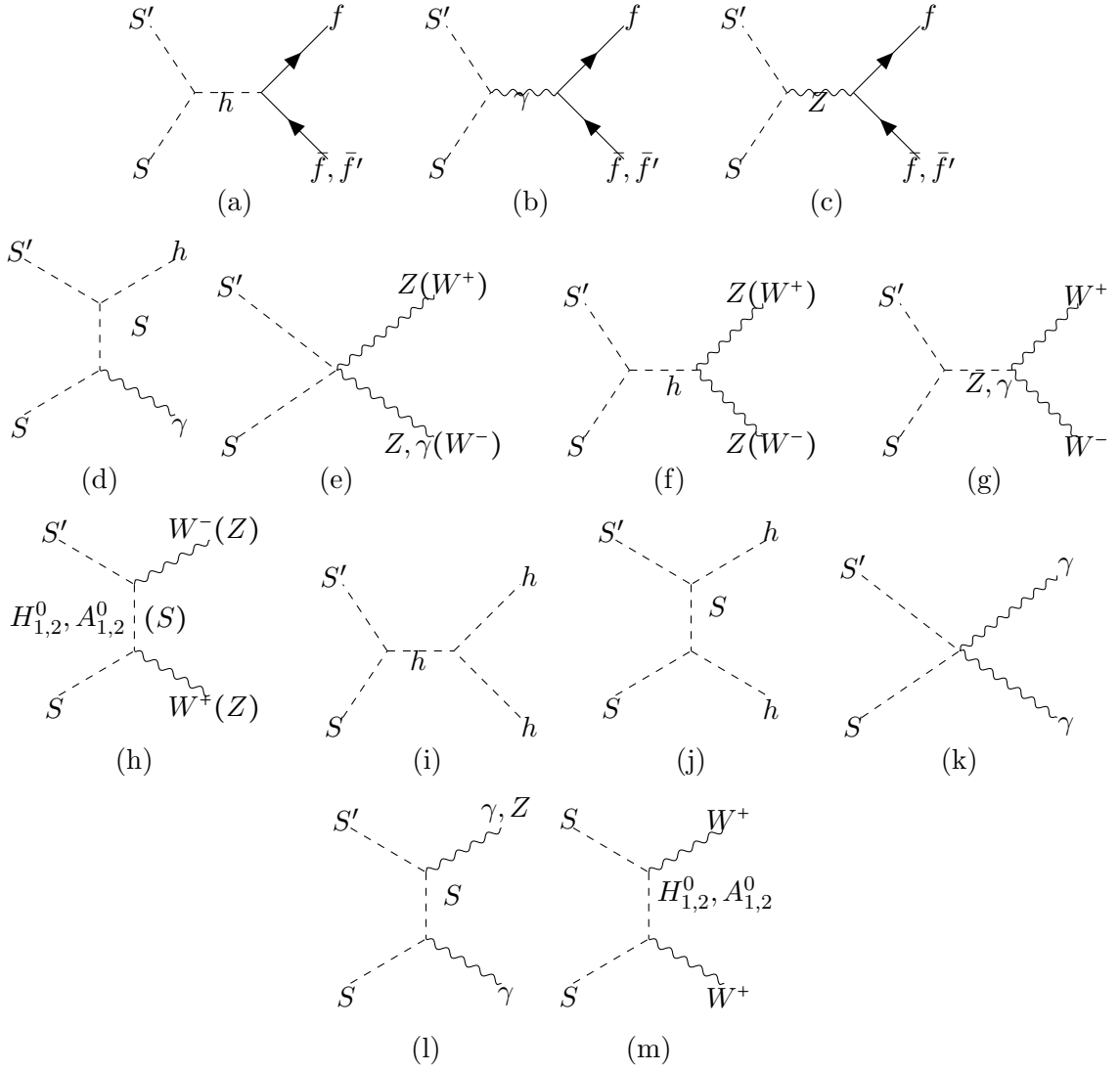


Figure 14: Co-annihilation channels for $S' = H_{1,2}^-$ and $S = H_{1,2}^+$, where f represent quark.

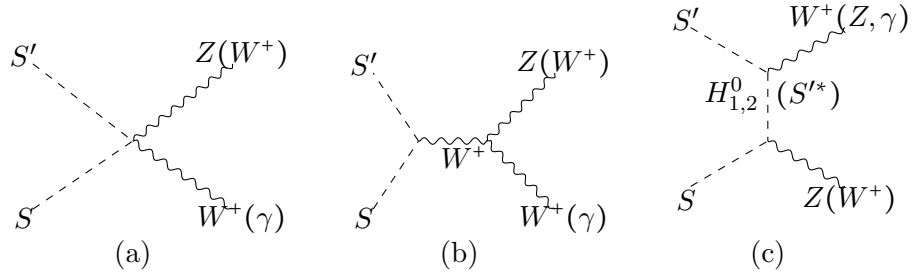


Figure 15: Co-annihilation channels for $S = H_{1,2}^0, A_{1,2}^0$ and $S' = H_{1,2}^+$.

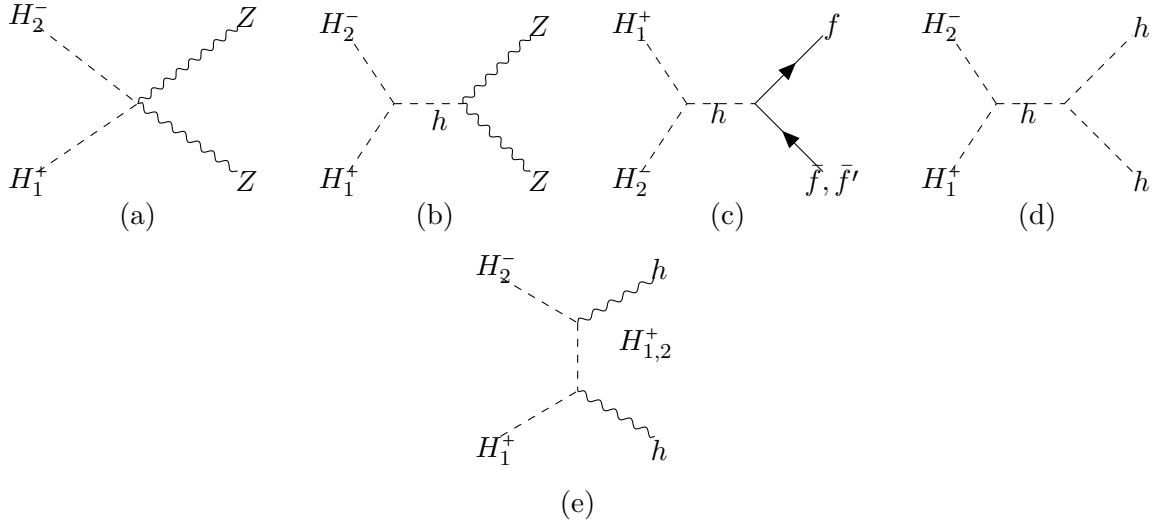


Figure 16: Dominating co-annihilation channels, where f represent quark.

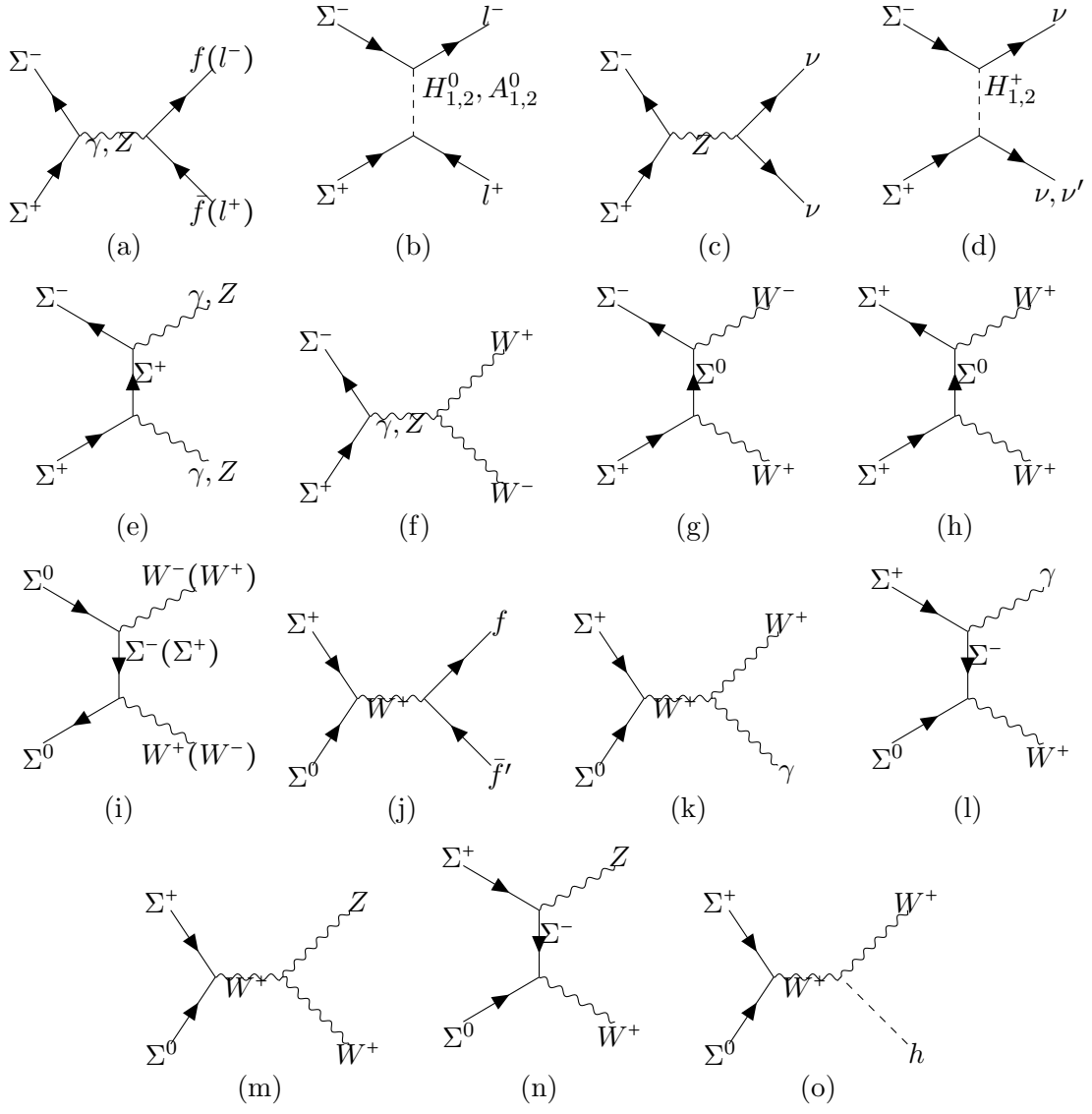


Figure 17: Dominating (co-)annihilation channels where f (l) represent quark (lepton).

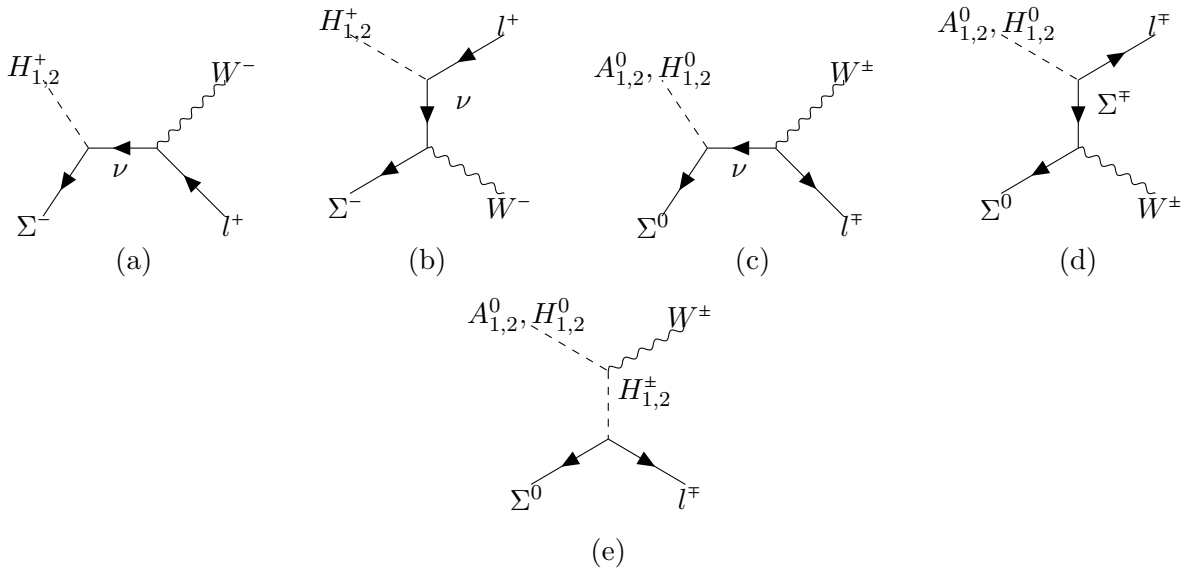


Figure 18: Dominating co-annihilation channels of triplet fermion with inert scalars where l represent lepton.

References

- [1] Y. Fukuda *et al.* [Super-Kamiokande], Phys. Rev. Lett. **81**, 1562-1567 (1998).
- [2] Q. R. Ahmad *et al.* [SNO], Phys. Rev. Lett. **87**, 071301 (2001).
- [3] Q. R. Ahmad *et al.* [SNO], Phys. Rev. Lett. **89**, 011301 (2002).
- [4] B. Aharmim *et al.* [SNO], Phys. Rev. C **88**, 025501 (2013).
- [5] N. Aghanim *et al.* [Planck], Astron. Astrophys. **641**, A6 (2020) [erratum: Astron. Astrophys. **652**, C4 (2021)].
- [6] E. Ma and D. Suematsu, Mod. Phys. Lett. A **24**, 583-589 (2009).
- [7] W. Chao, Int. J. Mod. Phys. A **30**, no.01, 1550007 (2015).
- [8] A. Ahriche, A. Jueid and S. Nasri, Phys. Rev. D **97**, no.9, 095012 (2018).
- [9] A. Ahriche, A. Arhrib, A. Jueid, S. Nasri and A. de La Puente, Phys. Rev. D **101**, no.3, 035038 (2020).
- [10] N. G. Deshpande and E. Ma, Phys. Rev. D **18**, 2574 (1978).
- [11] L. Lopez Honorez, E. Nezri, J. F. Oliver and M. H. G. Tytgat, JCAP **02**, 028 (2007).
- [12] M. Gustafsson, PoS **CHARGED2010**, 030 (2010).
- [13] A. Belyaev, G. Cacciapaglia, I. P. Ivanov, F. Rojas-Abatte and M. Thomas, Phys. Rev. D **97**, no.3, 035011 (2018).
- [14] A. Ilnicka, M. Krawczyk and T. Robens, Phys. Rev. D **93**, no.5, 055026 (2016).
- [15] A. Jueid, J. Kim, S. Lee, S. Y. Shim and J. Song, Phys. Rev. D **102**, no.7, 075011 (2020).
- [16] R. Basu, M. Pandey, D. Majumdar and S. Banerjee, Int. J. Mod. Phys. A **36**, no.23, 2150163 (2021).
- [17] J. Kalinowski, T. Robens, D. Sokolowska and A. F. Zarnecki, Symmetry **13**, no.6, 991 (2021).
- [18] J. E. Falaki, Phys. Lett. B **840**, 137879 (2023).
- [19] A. Ghosh, P. Konar and S. Seth, Springer Proc. Phys. **304**, 128-132 (2024).
- [20] A. Ghosh, P. Konar and S. Seth, Phys. Rev. D **105**, no.11, 115038 (2022).
- [21] H. Abouabid, A. Arhrib, A. Hmissou and L. Rahili, Eur. Phys. J. C **84**, no.6, 632 (2024).
- [22] A. Arhrib, Y. L. S. Tsai, Q. Yuan and T. C. Yuan, JCAP **06**, 030 (2014).

- [23] B. Eiteneuer, A. Goudelis and J. Heisig, Eur. Phys. J. C **77**, no.9, 624 (2017).
- [24] J. Kalinowski, W. Kotlarski, T. Robens, D. Sokolowska and A. F. Zarnecki, JHEP **12**, 081 (2018).
- [25] A. Datta, N. Ganguly, N. Khan and S. Rakshit, Phys. Rev. D **95**, no.1, 015017 (2017).
- [26] J. Aalbers *et al.* [LZ Collaboration], [arXiv:2410.17036 [hep-ex]].
- [27] E. Ma, Phys. Rev. D **73**, 077301 (2006).
- [28] T. Toma and A. Vicente, JHEP **01**, 160 (2014).
- [29] D. Borah, A. Dasgupta, K. Fujikura, S. K. Kang and D. Mahanta, JCAP **08**, 046 (2020).
- [30] L. Sarma, P. Das and M. K. Das, Nucl. Phys. B **963**, 115300 (2021).
- [31] Tapender, S. Verma and S. Kumar, Eur. Phys. J. Plus **140**, no.1, 43 (2025).
- [32] A. Beniwal, J. Herrero-García, N. Leerdam, M. White and A. G. Williams, JHEP **21**, 136 (2020).
- [33] Y. Farzan, Phys. Rev. D **80**, 073009 (2009).
- [34] A. Ahriche, K. L. McDonald and S. Nasri, JHEP **06**, 182 (2016).
- [35] S. Esch, M. Klasen and C. E. Yaguna, JHEP **10**, 055 (2018).
- [36] T. Cohen, J. Kearney, A. Pierce and D. Tucker-Smith, Phys. Rev. D **85**, 075003 (2012).
- [37] C. Cheung and D. Sanford, JCAP **02**, 011 (2014).
- [38] A. Dutta Banik and D. Majumdar, Eur. Phys. J. C **74**, no.11, 3142 (2014).
- [39] A. Ahriche, JHEP **02**, 028 (2023).
- [40] D. Hehn and A. Ibarra, Phys. Lett. B **718**, 988-991 (2013).
- [41] J. Fuentes-Martín, M. Reig and A. Vicente, Phys. Rev. D **100**, no.11, 115028 (2019).
- [42] B. Garbrecht and E. Wang, Phys. Rev. D **110**, no.11, 11 (2024).
- [43] P. Escribano, M. Reig and A. Vicente, JHEP **07**, 097 (2020).
- [44] M. Hirsch, R. A. Lineros, S. Morisi, J. Palacio, N. Rojas and J. W. F. Valle, JHEP **10**, 149 (2013).
- [45] P. Rocha-Moran and A. Vicente, JHEP **07**, 078 (2016).
- [46] J. Fiaschi, M. Klasen and S. May, JHEP **05**, 015 (2019).
- [47] S. Choubey, S. Khan, M. Mitra and S. Mondal, Eur. Phys. J. C **78**, no.4, 302 (2018).
- [48] A. Batra, S. K.A., S. Mandal and R. Srivastava, Int. J. Mod. Phys. A **38**, no.35n36, 2340003 (2023).

- [49] L. Singh, D. Mahanta and S. Verma, JCAP **02**, 041 (2024).
- [50] S. Ashanujjaman and K. Ghosh, Phys. Lett. B **825**, 136889 (2022).
- [51] G. Aad *et al.* [ATLAS], Eur. Phys. J. C **81**, no.3, 218 (2021).
- [52] A. M. Sirunyan *et al.* [CMS], JHEP **03**, 051 (2020).
- [53] J. A. Casas and A. Ibarra, Nucl. Phys. B **618**, 171-204 (2001).
- [54] K. Kannike, Eur. Phys. J. C **72**, 2093 (2012).
- [55] K. Kannike, Eur. Phys. J. C **76**, no.6, 324 (2016) [erratum: Eur. Phys. J. C **78**, no.5, 355 (2018)].
- [56] K. Kannike, Eur. Phys. J. C **81**, no.10, 940 (2021).
- [57] A. Ahriche, G. Faisel, S. Y. Ho, S. Nasri and J. Tandean, Phys. Rev. D **92**, no.3, 035020 (2015).
- [58] A. G. Akeroyd, A. Arhrib and E. M. Naimi, Phys. Lett. B **490**, 119-124 (2000).
- [59] J. Abdallah *et al.* [DELPHI], Eur. Phys. J. C **31**, 421-479 (2003).
- [60] E. Lundstrom, M. Gustafsson and J. Edsjo, Phys. Rev. D **79**, 035013 (2009).
- [61] A. Pierce and J. Thaler, JHEP **08**, 026 (2007).
- [62] A. M. Baldini *et al.* [MEG], Eur. Phys. J. C **76**, no.8, 434 (2016).
- [63] S. Navas *et al.* [Particle Data Group], Phys. Rev. D **110**, no.3, 030001 (2024)
- [64] I. Esteban, M. C. Gonzalez-Garcia, M. Maltoni, I. Martinez-Soler, J. P. Pinheiro and T. Schwetz, JHEP **12**, 216 (2024).
- [65] F. Staub, [arXiv:0806.0538 [hep-ph]].
- [66] F. Staub, Comput. Phys. Commun. **185**, 1773-1790 (2014).
- [67] F. Staub, Adv. High Energy Phys. **2015**, 840780 (2015).
- [68] W. Porod, F. Staub and A. Vicente, Eur. Phys. J. C **74**, no.8, 2992 (2014).
- [69] W. Porod, Comput. Phys. Commun. **153**, 275-315 (2003).
- [70] W. Porod and F. Staub, Comput. Phys. Commun. **183**, 2458-2469 (2012).
- [71] G. Belanger, F. Boudjema, A. Pukhov and A. Semenov, Comput. Phys. Commun. **149**, 103-120 (2002).
- [72] G. Belanger, A. Mjallal and A. Pukhov, Eur. Phys. J. C **81**, no.3, 239 (2021).

- [73] G. Belanger, A. Bharucha, B. Fuks, A. Goudelis, J. Heisig, A. Jueid, A. Lessa, K. A. Mohan, G. Polesello and P. Pani, *et al.* JHEP **02**, 042 (2022).
- [74] G. Alguero, G. Belanger, S. Kraml and A. Pukhov, SciPost Phys. **13**, 124 (2022).
- [75] G. Bélanger, F. Boudjema, A. Pukhov and A. Semenov, Comput. Phys. Commun. **192**, 322-329 (2015).
- [76] K. Griest and D. Seckel, Phys. Rev. D **43**, 3191-3203 (1991).
- [77] V. Keus, S. F. King, S. Moretti and D. Sokolowska, JHEP **11**, 003 (2015).
- [78] J. Aalbers *et al.* [LZ], Phys. Rev. Lett. **131**, no.4, 041002 (2023).
- [79] D. S. Akerib *et al.* [LUX], Phys. Rev. Lett. **118**, no.2, 021303 (2017).
- [80] Y. Meng *et al.* [PandaX-4T], Phys. Rev. Lett. **127**, no.26, 261802 (2021).
- [81] E. Aprile *et al.* [XENON], Phys. Rev. Lett. **131**, no.4, 041003 (2023).
- [82] E. Aprile *et al.* [XENON], Phys. Rev. Lett. **121**, no.11, 111302 (2018).
- [83] R. Ajaj *et al.* [DEAP], Phys. Rev. D **100**, no.2, 022004 (2019).
- [84] C. A. J. O'Hare, Phys. Rev. Lett. **127**, no.25, 251802 (2021).
- [85] R. Franceschini, T. Hambye and A. Strumia, Phys. Rev. D **78**, 033002 (2008).
- [86] F. von der Pahlen, G. Palacio, D. Restrepo and O. Zapata, Phys. Rev. D **94**, no.3, 033005 (2016).
- [87] J. Kalinowski, W. Kotlarski, T. Robens, D. Sokolowska and A. F. Zarnecki, JHEP **07**, 053 (2019).
- [88] S. Baumholzer, V. Brdar, P. Schwaller and A. Segner, JHEP **09**, 136 (2020).
- [89] J. Liu, Z. L. Han, Y. Jin and H. Li, JHEP **12**, 057 (2022).
- [90] A. Das and S. Mandal, Nucl. Phys. B **966**, 115374 (2021).
- [91] T. Li, H. Qin, C. Y. Yao and M. Yuan, Phys. Rev. D **106**, no.3, 035021 (2022).
- [92] L. Singh, R. Srivastava, S. Verma and S. Yadav, [arXiv:2501.13171 [hep-ph]].
- [93] M. Aicheler *et al.* [CLIC accelerator], doi:10.23731/CYRM-2018-004 [arXiv:1903.08655 [physics.acc-ph]].
- [94] P. Bambade, T. Barklow, T. Behnke, M. Berggren, J. Brau, P. Burrows, D. Denisov, A. Faus-Golfe, B. Foster and K. Fujii, *et al.* [arXiv:1903.01629 [hep-ex]].
- [95] G. Apollinari, I. Béjar Alonso, O. Brüning, M. Lamont and L. Rossi, doi:10.5170/CERN-2015-005.
- [96] A. Abada *et al.* [FCC], Eur. Phys. J. ST **228**, no.4, 755-1107 (2019).

- [97] C. Degrande, C. Duhr, B. Fuks, D. Grellscheid, O. Mattelaer and T. Reiter, Comput. Phys. Commun. **183**, 1201-1214 (2012).
- [98] J. Alwall, R. Frederix, S. Frixione, V. Hirschi, F. Maltoni, O. Mattelaer, H. S. Shao, T. Stelzer, P. Torrielli and M. Zaro, JHEP **07**, 079 (2014).